Three-dimension modeling of direct-drive cryogenic implosions on OMEGA

I. V. Igumenshchev, V. N. Goncharov, F. J. Marshall, J. P. Knauer, E. M. Campbell, D. H. Froula, R. L. McCrory, S. P. Regan, T. C. Sangster, and S. Skupsky

Laboratory for Laser Energetics, University of Rochester 250 East River Road, Rochester, NY 14623, USA

Abstract

The effects of large-scale (with Legendre modes $\lesssim 10$) laser-imposed nonuniformities in direct-drive cryogenic implosions on the OMEGA laser system are investigated using three-dimension hydrodynamic simulations performed using a newly developed code ASTER. Sources of these nonuniformities include an illumination pattern produced by 60 OMEGA laser beams, capsule offsets ($\sim$ 10 to 20 μm), and imperfect pointing, energy balance, and timing of the beams (with typical $\sigma_{rms} \sim 10$ μm, 10%, and 5 ps, respectively). Two implosion designs using 26-kJ triple-picket laser pulses were studied: a nominal design, in which a 880-μm-diameter capsule is illuminated by the same-diameter beams, and a "R75" design using a capsule of 900 μm in diameter and beams of 75% of this diameter. Simulations found that nonuniformities because of capsule offsets and beam imbalance have the largest effect on implosion performance. These nonuniformities lead to significant distortions of implosion cores resulting in an incomplete stagnation. The shape of distorted cores is well represented by neutron images, but loosely in x-rays. Simulated neutron spectra from perturbed implosions show large directional variations and up to $\sim$ 2 keV variation of the hot spot temperature inferred from these spectra. The R75 design is more hydrodynamically efficient because of mitigation of crossed-beam energy transfer, but also suffers

more from the nonuniformities. Simulations predict a performance advantage of this design over the nominal design when the target offset and beam imbalance σ_{rms} are reduced to less than 5 μm and 5%, respectively.

I. INTRODUCTION

Direct-drive cryogenic implosion experiments on the 30-kJ OMEGA laser system[1] are armed on demonstration of hydrodynamic equivalence of scaled-down inertial confinement fusion (ICF) experiments to ignition ICF experiments.[2,3] This requires to employ low-adiabat ($\alpha < 3$, where the adiabat α is the ratio of the pressure to Fermi-degenerated pressure of a DT fuel), high-convergence-ratio cryogenic implosion designs, which demonstrate maximum performance in idealized one-dimensional (1D) spherically symmetric simulations.[4] Experimental study of these designs on OMEGA using the reflection light diagnostic[5] and shell trajectory measurements[6] found that the dynamics of implosion shells during the acceleration stage is in good agreement with 1D predictions using the ICF code LILAC.[7] LILAC considers all major physical effects in implosion targets including nonlocal thermal transport[8] and crossed-beam energy transfer (CBET).[9] The overall performance of such designs, however, is far below the predicted one, showing a reduction of the measured neutron yield by 70% to 90% and reduction of the inferred hot spot pressure by about 50%.[4]

This good agreement between measured and simulated laser coupling of the low-adiabat implosions on one side and overall underperfomance of these implosions on other side suggests an importance of three-dimensional (3D) effects, which are expected to develop at the deceleration implosion stage[2] because of the secular (for the Legendre modes ℓ from 1 to ~ 3) and Rayleigh-Taylor[10] (for $\ell \gtrsim 10$) growths. The presence of the 3D effects is confirmed by observations of low-mode nonuniformities in implosion targets obtained using x-ray imaging[11] and neutron diagnostics.[12] Simulations of OMEGA implosions employing the two-dimension (2D) ICF code DRACO[13] have demonstrated that the implosion performance can suffer form nonuniformities sourced by target offsets (measured with respect to the laser beam pointing center), mount stalks, target surface defects, and nonuniform laser irradiation (e.g., Refs

[14, 15]). Such simulations, however, were limited to only axisymmetric perturbations and can not reproduce the full 3D nature of real implosions.

There are almost two decade long extensive efforts of simulating indirect- and direct-drive ICF implosions using 3D radiation-hydrodynamic code HYDRA.[16] Recent HYDRA simulations of indirect-drive implosions were focused on modeling high and low ℓ-mode nonuniformities from sources as in real high compression implosions on the National Ignition Facility (NIF).[17] These sources include target surface imperfections, radiation drive asymmetries, fill tubes, and capsule support tents.[18] Simulations suggest that several kJ of energy in the cores of NIF implosion targets remains as unstagnated kinetic energy. This results in undercompression and reduction of the performance of these implosions.[19] The incomplete stagnation seen in the simulations is confirmed by a temporal and spatial evolution of x-ray and neutron images of implosion cores. These images show good agreements with the evolution found in simulations.[20, 21]

HYDRA simulations of direct-drive implosions were focused on studding a polar drive configuration[22] on the NIF and OMEGA laser facility.[23, 24] These simulations, as well as 2D DRACO simulations,[25] allow to predict and better control large-scale nonuniformities (mostly with $\ell = 2$ and 4) imposed by the polar drive.

In this paper, the evolution and effects of large-scale laser-imposed nonuniformities (with $\ell \lesssim 10$) in cryogenic OMEGA implosions are investigated using a newly developed 3D ICF code ASTER. This code is an eulerian one, optimized for direct-drive implosions, and implemented on a simple spherical grid, which allows to preserve spherical symmetry of uniform implosions with a high accuracy. The code does not require significant computational resources and runs relatively fast. ASTER can consider nonuniformities caused by the 60 OMEGA laser beam irradiation ("beam overlap" perturbations), and because of imperfect pointing, energy balance, and timing of these beams. In addition, nonuniformities introduced by target offsets can be

considered. The latter nonuniformities change the global symmetry of the irradiation pattern and results in perturbations with the dominant $\ell = 1$-mode.

Beam overlapping in the OMEGA laser with its 60-beam configuration forming a truncated icosahedron (soccer ball) typically introduces perturbations with the dominant ℓ- and m-modes equal to 10. These modes slowly develop and do not play any significant role during the acceleration stage, and can become large and important during formation of the hot spot. Mispointing, imbalance, and mistiming of each individual beam are unintentionally introduced because of OMEGA hardware limitations and typically have $\sigma_{\rm rms} \sim 10$ μm, 10%, and 5 ps for beam mispointing, imbalance, and mistiming, respectively. These sources of nonuniformities are quasi random and result in on-target irradiation perturbations with broad spectra, which peak at the lowest ℓ-modes from 1 to ~ 3 and gradually decline toward higher ℓ-modes. Target offsets are also unintentionally introduced, randomly directed, and typically measure from about 10 to 20 μm. Perturbations developed from the mentioned sources are truly 3D, interacting and competing with each other on the linear and nonlinear evolution stages. This results in complicated target structures, which affect the implosion dynamics during the maximum compression and reduces the overall implosion performance. It is essential, therefore, to accurately predict effects of these perturbations in full 3D.

A mount stalk are another important source of nonuniformities in direct-drive implosions. Such a stalk develops a jet-like structure penetrating and perturbing the hot spot.[14] ASTER can not simulate mount stalks consistently because of current capability limitations. Instead, the effects of the stalks were simulated assuming surrogate perturbations, which mimic the perturbations of implosion shells from the stalk similar to that found in the consistent 2D DRACO simulations of implosions with the stalk. Understanding nonlinear interactions of perturbations from the stalks and other sources of nonuniformities in 3D is important as it can result in a cumulative

enhancement of such perturbations.

Approaching ignition-relevant conditions in direct-drive ICF implosions requires achieving hot spot pressure in excess of 100 Gbar.[4] According to 1D predictions, such a pressure in implosions without mitigation of CBET[26] can be rigidly developed in low-adiabat ($\alpha \lesssim 3$) cryogenic implosions and marginally in mid-adiabat ($\alpha \sim 4$) ones. Current low-adiabat cryogenic implosions on OMEGA measure the pressure of about 20 to 30 Gbar and mid-adiabat ones measure up to about 60 Gbar. The most significant factor limiting the performance of low-adiabat implosions is likely small-scale hydrodynamic mixing of the ablator material (CD) into the hot spot formed by a DT plasma. This mix can be sourced either by laser imprint[27] or surface defects,[28] or by both. Complete avoiding these sources is technically difficult problem. The mid-adiabat implosions should be more stable with respect to perturbations resulting in the mix, but they likely suffer from low ℓ-mode perturbations from laser (beam overlap, imbalance, etc.) and target nonuniformities. To achieve the 100 Gbar pressure goal, performance of OMEGA implosions can be improved by the following two-fold way: first, employing mid-adiabat implosions to reduce or eliminate the small-scale mix, and second, extending the performance margin of mid-adiabat implosions by mitigating CBET losses. The latter should also be accompanied by a reduction of the low ℓ-mode perturbations.

Two cryogenic implosion designs are considered in this paper. One is a nominal design, which is similar to OMEGA shot 78378, and other is a more hydrodynamically efficient design utilizing mitigation of CBET by using fixed small-diameter laser beams with $R_b/R_t = 0.75$, where R_b and R_t are the radii of the beams and target, respectively, and the former radius is defined as the one incirculating 95% beam energy. Both designs are mid-adiabat ones and their performances are tested and compared assuming various laser-imposed low ℓ-mode perturbations. The design utilizing mitigation of CBET has the potential to achieve the 100 Gbar pressure goal

and is nicknamed as the "R75" design.

This paper is organized as follows: Section II describes the code ASTER. Simulations of two cryogenic OMEGA implosion designs, the nominal and R75 ones, are presented Sec. III. The results of these simulations are discussed and concluded in Sec. IV.

II. THE CODE ASTER

ASTER is a 3D eulerian hydrodynamic code, which was developed specifically for direct-drive ICF applications. The code simulates the evolution of plasma flows considering the two-temperature (for ions and electrons) fluid plasma model. Plasma can consist of different materials, which are considered as separate media having, however, the same velocity (single-fluid approximation). Spatial distributions of hydrodynamic quantities are defined using the spherical orthogonal grid (R, θ, ϕ), except the momentum components are expressed using the cartesian coordinates, $\mathbf{M} = (M_x, M_y, M_z)$. Such a two coordinate approach eliminates the "fiction" Coriolis and centrifugal force terms in the equation of momentum. The code employs the hydrodynamic equations in the following form:

the mass conservation equation for each material α,

$$\frac{\partial \rho^\alpha}{\partial t} + \nabla \cdot (\rho^\alpha \mathbf{u}) = 0, \tag{1}$$

the equations for three momentum components,

$$\begin{aligned} \frac{\partial M_x}{\partial t} + \nabla \cdot (M_x \mathbf{u}) &= -(\nabla P)_x, \\ \frac{\partial M_y}{\partial t} + \nabla \cdot (M_y \mathbf{u}) &= -(\nabla P)_y, \\ \frac{\partial M_z}{\partial t} + \nabla \cdot (M_z \mathbf{u}) &= -(\nabla P)_z, \end{aligned} \tag{2}$$

the total (ions and electrons) energy equation,

$$\frac{\partial E}{\partial t} + \nabla \cdot [(E + P)\mathbf{u} + \mathbf{q}_\mathrm{i} + \mathbf{q}_\mathrm{e}] = S_\mathrm{e}, \tag{3}$$

and the electron energy equation,

$$\frac{\partial \rho \epsilon_{\rm e}}{\partial t} + \nabla \cdot (\rho \epsilon_{\rm e} \mathbf{u} + \mathbf{q}_{\rm e}) = -P_{\rm e} \nabla \cdot \mathbf{u} + J + S_{\rm e}. \tag{4}$$

Here, $\rho = \sum_\alpha \rho^\alpha$ is the total density of a multi-material medium, ρ^α is the average cell density of the material α, $\mathbf{u} = \mathbf{M}/\rho$ is the velocity, $P = P_{\rm i} + P_{\rm e}$ is the plasma pressure, $P_{\rm i}$ and $P_{\rm e}$ are the ion and electron pressure, $E = \rho\epsilon_{\rm i} + \rho\epsilon_{\rm e} + u^2/2$ is the plasma energy density, $\epsilon_{\rm i}$ and $\epsilon_{\rm e}$ are the specific internal energies of ions and electrons, $\mathbf{q}_{\rm i}$ and $\mathbf{q}_{\rm e}$ are the ion and electron heat fluxes, $S_{\rm e}$ is the heat source for electrons, and the term J describes the energy exchange between electrons and ions. The operator ∇, when applied to a vector, denotes the divergency in the spherical coordinates,

$$\nabla \cdot \mathbf{A} = \frac{1}{R^2}\frac{\partial (R^2 A_r)}{\partial R} + \frac{1}{R\sin\theta}\frac{\partial (A_\theta \sin\theta)}{\partial \theta} + \frac{1}{R\sin\theta}\frac{\partial A_\phi}{\partial \phi}, \tag{5}$$

and, when applied to a scalar, denotes the gradient in the spherical coordinates,

$$\nabla A = \left(\frac{\partial A}{\partial R}, \frac{1}{R}\frac{\partial A}{\partial \theta}, \frac{1}{R\sin\theta}\frac{\partial A}{\partial \phi} \right). \tag{6}$$

The standard relations between vector components in the spherical and cartesian coordinates are used to express corresponding velocity and ∇P components in eqs. (1)-(4).

Equations (1)-(4) are completed by the equations of state for each material α including electron and ion components,

$$P_{\rm i}^\alpha = P_{\rm i}^\alpha(\rho^\alpha, T_{\rm i}), \qquad P_{\rm e}^\alpha = P_{\rm e}^\alpha(\rho^\alpha, T_{\rm e}), \tag{7}$$

$$\epsilon_{\rm i}^\alpha = \epsilon_{\rm i}^\alpha(\rho^\alpha, T_{\rm i}), \qquad \epsilon_{\rm e}^\alpha = \epsilon_{\rm e}^\alpha(\rho^\alpha, T_{\rm e}), \tag{8}$$

where $T_{\rm i}$ and $T_{\rm e}$ are the ion and electron temperatures. When a mixture of materials is considered, the density ρ^α in eqs.. (7) and (8) should be substituted by ρ^α/f^α, where f^α is the fractional volume occupied by the material α. By definition, $\sum_\alpha f^\alpha = 1$.

The ion and electron pressures of a material mix are then approximately determined as a waited average of the pressures of all materials,

$$P_{\mathrm{i}} = \sum_{\alpha} f^{\alpha} P_{\mathrm{i}}^{\alpha}, \qquad P_{\mathrm{e}} = \sum_{\alpha} f^{\alpha} P_{\mathrm{e}}^{\alpha}, \tag{9}$$

and the ion and electron internal energy densities are defined as

$$\rho\epsilon_{\mathrm{i}} = \sum_{\alpha} \rho^{\alpha} \epsilon_{\mathrm{i}}^{\alpha}, \qquad \rho\epsilon_{\mathrm{e}} = \sum_{\alpha} \rho^{\alpha} \epsilon_{\mathrm{e}}^{\alpha}. \tag{10}$$

The fractional volume f^{α} can be defined using different approximations; the one used in this paper is explained in Appendix A.

ASTER utilizes the process splitting approach when contributions of different physical processes to the whole evolution are considered separately. This means that at each timestep Δt the processes are consequently calculated one after other and locally independent of each other. Currently, the code contains three main blocks representing three physical processes: the hydrodynamic block, electron and ion thermal transport and temperature equilibration block, and laser deposition block. In addition to those, several "diagnostic" processes, which do not affect the evolution of the system, are calculated. Currently, the diagnostic processes include DD and DT fusion reactivities, neutron spectrum calculations,[29] optically thin x-ray imaging due to plasma self-emission, and neutron imaging.

The hydrodynamic block in ASTER employs the explicit, finite-difference piecewise-parabolic method (PPM) by Colella & Woodward.[30] The version of PPM called "eulerian" is implemented. PPM is a Godunov-type method and requires solving the Riemann problem at numerical zone interfaces.[31] The code uses an iterative Riemann solver, which takes into consideration equations of state for real gases[32] [eqs. (7) and (8)].

3D hydrodynamics is implemented in ASTER using the dimension split approach, in which 1D versions of eqs. (1)-(4) (with the terms related only to the hydrodynamic

block) are consequently solved for each dimension R, θ, and ϕ. Test simulations showed that choosing a specific order of the dimension sequence (assuming a uniform alternation of these dimensions in consequent timesteps) has small effect on the results.

The timestep Δt in ASTER is limited by the hydrodynamic Courant stability criterion,[33]

$$\Delta t < \frac{\min\left(\Delta R, R\Delta\theta, R\sin\theta\Delta\phi\right)}{u + c_{\rm s}}, \tag{11}$$

where c_s is the sound speed, and ΔR, $\Delta\theta$, and $\Delta\phi$ are the sizes of numerical zones in the corresponding dimension. In the case of full-sphere simulations, an application of the criterion (11) can result in a significant reduction of Δt because of small sizes of the zones in the ϕ- and θ-dimensions near the grid center and polar axis. This problem is solved in ASTER employing a "macrozoning" technique. In this technique, the hydrodynamic conservative quantities ρ^{α}, $\mathbf{M}$, $\rho\epsilon_{\rm i}$, and $\rho\epsilon_{\rm e}$ are remapped from a fine to course grid in the ϕ- and θ-dimensions before performing the corresponding 1D hydrodynamic calculations, so that flows can be advanced in simulations using a relatively large Δt. After completing these calculations, the mentioned hydrodynamic quantities are remapped back to the original grid structure. The remapping between different grids is performed using the piecewise-parabolic interpolation scheme adopted form PPM. The use of the dimension split approach simplifies the implementation of macrozoning, which then requires only 1D remapping. In this case, the macrozoning in θ- or ϕ-dimension is applied concurrently with the corresponding 1D hydrodynamic sweep.

The thermal transport block in ASTER solves the following energy equations for electrons and ions neglecting motions of the plasma,

$$\rho c_{v{\rm e}}\frac{\partial T_{\rm e}}{\partial t} = -\nabla\cdot\mathbf{q}_{\rm e} + J + S_{\rm e} \tag{12}$$

and

$$\rho c_{v\mathrm{i}} \frac{\partial T_{\mathrm{i}}}{\partial t} = -\nabla \cdot \mathbf{q}_{\mathrm{i}} - J, \tag{13}$$

where $c_{v\mathrm{e}}$ and $c_{v\mathrm{i}}$ are the electron and ion specific heats at constant volume,

$$J = \rho c_{v\mathrm{e}} \frac{T_{\mathrm{i}} - T_{\mathrm{e}}}{\tau_{\mathrm{ei}}} \tag{14}$$

is the electron and ion temperature equilibration term, and τ_{ei} is the electron-ion temperature equilibration time.[34] The heat fluxes in eqs. (12) and (13) are defined as

$$\mathbf{q}_{\mathrm{e}} = -\kappa_{\mathrm{e}} \nabla T_{\mathrm{e}}, \tag{15}$$

and

$$\mathbf{q}_{\mathrm{i}} = -\kappa_{\mathrm{i}} \nabla T_{\mathrm{i}}, \tag{16}$$

where κ_{e} and κ_{i} are the electron and ion thermal conductivity coefficients. ASTER employs the Spitzer-Härm thermal conduction model[35] for both electrons and ions. Equations (12) and (13) are solved using the dimension split approach and integrated over time using the fully implicit finite-difference scheme, which is stable for any grid size and timestep.

The laser deposition block in ASTER calculates absorption of laser light in corona of implosion targets. This process is represented by the source S_{e} in eqs. (3) and (4). The code employs a simplified 3D model of laser deposition, in which the corona is treated as a spherically symmetric one but sources of laser light (laser beams) can be nonuniformly distributed around a target and have different energy, pointing, and history. Test simulations have shown that the outer sub-critical part of the corona (in which $n_{\mathrm{e}} < n_{\mathrm{c}}$, where n_{e} is the electron number density and $n_{\mathrm{c}} = 9 \times 10^{21}$ cm^{-3} is the critical density corresponding to OMEGA laser light) is hot ($T_{\mathrm{e}} \sim 1$ keV) and highly thermal conductive that result in efficient smoothing temperature and density nonuniformities in the θ- and ϕ-directions even in the case of significant distortions

of implosion shells. This justifies the accuracy of the simplified spherical symmetry assumption.

ASTER adopts a laser deposition routing form LILAC with some modifications. This routine calculates the spatial distribution of the absorbed laser energy in a 1D target corona from a single laser beam. The routine employs the ray-trace model for propagation of light and assumes laser absorption because of inverse bremsstrahlung. It also includes the effects of CBET assuming that implosion targets are uniformly illuminated by laser.[9] The found single-beam distribution of laser absorption is then used to compose a 3D 60-beam laser deposition pattern around a target taking into account the OMEGA beam-port geometry. The coordinates of the beam ports in the spherical system adopted in ASTER are presented in Appendix B. The laser beam energy imbalance, mispointing, and mistiming can be simulated assuming corresponding perturbations of the individual beam's energy, pointing, and timing. The target offset can be modeled shifting single-beam absorption patterns in accordance with repointing the beams to a desired offset center.

ASTER simulations presented in this paper use the full Spitzer thermal transport (i.e., without applying the flux-limiter $f \sim 0.1$[36]). The validity of this approach was confirmed by LILAC test simulations of triple-picket cryogenic implosion designs using the laser deposition model with CBET and either the nonlocal or Spitzer thermal transport model. These simulations showed close agreement, which indicates that the use of flux-limitation is actually motivated by the need to mimic CBET losses in simplified implosion simulations without CBET. An important difference between the nonlocal and Spitzer models was only noticed during the 1st picket, when the latter model somewhat overestimates the inward thermal flux resulting in a stronger 1st shock propagating through the plastic/DT-ice shell. This problem can be fixed, for example, reducing the energy of the 1st picket by about 10%.

ASTER is designed for parallel multi-processor simulations implementing the

domain-decomposition approach. The code employs the message passing interface (MPI) libraries for inter-process communications. Full-sphere simulations presented in this paper mostly use a nominal-resolution grid of about $700 \times 60 \times 120$ points (in R-, θ-, and ϕ-dimensions, respectively). In some cases, a high-resolution grid of about $700 \times 120 \times 240$ points was employed and a comparison of simulations using this and nominal-resolution grid showed good convergence of results. The grid is divided onto 96 sub-domains, which are distributed over 96 processors. The parallel calculations are performed only in the hydrodynamic and thermal transport blocks of the code, and the laser deposition block is currently calculated using a single processor. A simulation of the typical cryogenic OMEGA implosion using the nominal-resolution grid takes less than 48 hours on the Laboratory for Laser Energetic's computer cluster.

III. SIMULATION RESULTS

Simulations of two $\alpha = 4$ implosion designs are discussed in this section. The first design is the nominal one corresponding to cryogenic OMEGA shot 78378. The implosion is driven by laser beams with the radius about equal to the initial target radius, $R_{\rm b}/R_{\rm t} \approx 1$. The beam intensity profile can be approximately represented by a supergaussian with the index $N_{SG} \approx 5$. These beam radius and beam profile were chosen to minimize beam overlap deposition nonuniformities. The second design is the perspective high performance R75 design, utilizing improved laser coupling through mitigating CBET losses. This design employs reduced-size laser beams with $R_{\rm b}/R_{\rm t} = 0.75$ that results in increased beam overlap nonuniformities.

A. The nominal design

Figure 1(a) shows the target structure and laser pulse of shot 78378. The target consists of a 51-μm DT-ice shell overcoated with a 7.8-μm plastic (CD) ablator and

has the overall diameter of 880 μm. The laser pulse includes three pickets followed by a gradually rising 1-ns main pulse with a step pre-pulse. The use of such a three-picket pulse allows better controlling shock timing and implosion adiabats.[37] Without mixing, the plastic shell is ablated off near end of the laser pulse leaving an all-DT implosion shell. This design is an example of medium-adiabat OMEGA implosion designs, which offer an improved performance with respect to that for low-adiabat ($\alpha \lesssim 3$) implosions because of better stability to short-wavelength (with $\ell \gtrsim 50$) Rayleigh-Taylor growth during the shell acceleration.[4] The short-wavelength perturbations can result in puffing up implosion shells (therefore, effective increasing the shell adiabat)[38] and injection of the ablator material (CD) into the hot spot.[28]

The total on-target energy in shot 78378 was about 26 kJ with the main drive intensity of about 10^{15} W/cm^2. Polarization smoothing (PS)[39] and smoothing by spectral dispersion (SSD)[40] were applied to mitigate laser imprint. The laser beams were shaped using SG5 phase plates, which produce almost round spots with the intensity distribution $\sim \exp\left[-(r/r_0)^{4.45}\right]$, where r is the radius from the center of the spot and $r_0 = 360.0$ μm. An estimate result in $R_\mathrm{b}/R_\mathrm{t} = 0.93$, which means that this implosion has relatively high CBET losses ($\sim 30\%$ of absorbed power).[26] The uniform (1D) implosion yields 2.27×10^{14} neutrons. Table 1 lists selected ASTER simulations of this design showing assumed sources of nonuniformities and predicted performance.

1. Beam overlap perturbations

Figure 2 show the equatorial and meridional cross-sections of the distributions of density ρ and ion temperature T_i in Model A1 (see Table 1) at peak neutron production, $t = 2.57$ ns. This model includes only effects of the OMEGA beam-port geometry. The 60 OMEGA ports are arranged in pentagons and hexagons forming

vertexes of a truncated icosahedron. The polar axis of the coordinate system goes through the centers of two opposed pentagons and the equatorial plane crosses 10 of the total 20 hexagons (see Appendix B for the ports' arrangement). The meridional cross-sections of simulated models shown hereafter are taken at $\phi = 0$.

The dense shell in the equatorial cross-section [Fig. 2(a)] shows small, barely noticeable perturbations at the inner edge with the dominant $m = 10$-mode. Perturbations of the shell look a little larger in the meridional cross-section [Fig. 2(b)]. The distributions of T_i in the hot spot [Figs. 2(c) and 2(d)] are highly spherically symmetric and just slightly perturbed because of the ports' illumination at the lower-temperature edges. The performance of this implosion insignificantly suffers showing the relative neutron yield $YOU = 0.99$ ("yield over uniform," or the yield of a perturbed implosion over the yield of the corresponding uniform implosion). Other characteristics of the model, the neutron averaged pressure at the peak neutron production, or hot spot pressure P_{hs}, and neutron averaged ion temperature $(T_i)_n$ are also very close to the corresponding 1D values (see Table 1, Models A0 and A1).

2. Perturbations from all sources

Target offset can be a source of important performance degradation of OMEGA implosions.[14] Figures 3(a) and 3(c) illustrate the effect of a 10-μm offset in the equatorial plane in Model A2, which, like Model A1, includes the beam overlap perturbations. The offset results in shifting the geometric center of the stagnated shell on a distance that about equals to the offset ($\sim$ 10 μm) in the same direction as the direction of the offset. The density distribution in the shell becomes asymmetric with mass predominantly accumulating in the hemisphere that is opposite to the direction of the offset [Fig. 3(a)].

The offset produces a narrow jet-like flow in the hot spot. This results from

several consequent bounced shocks that converge off the target center and create a high-velocity flow in the direction of the offset. The jet accumulates enough energy and momentum to "drill" a relatively small-diameter hole in the shell [Fig. 3(a)]. A part of the hot spot plasma, including plasma produced by the initial DT vapor [the interface of DT vapor is indicated by the black line in Fig. 3(a)], is escaping through this hole. The distribution of T_i in the hot spot is distorted accordingly forming a high-temperature feature in the direction of the jet [Fig. 3(c)]. The implosion performance is reduced quite substantially because of this 10-μm offset: the neutron yield drops by about 40% and the hot spot pressure P_{hs} by about 17% (see Table 1).

Beam imbalance, mispointing, and mistiming are quasi-random perturbations, but their distributions over OMEGA beams are approximately repeated from shot to shot. These perturbations result in nonuniformities of the laser deposition, which are characterized by broad-band spectra peaking at low ℓ- and m-modes, typically from 1 to 3, and gradually declining toward higher modes. Direct on-target measurement of beam imbalance and mispointing in OMEGA implosions is a difficult problem and, therefore, these quantities are estimated employing indirect measurements,[41] which suggest the beam imbalance $\sigma_{rms} \approx 10\%$ and the beam mispointing $\sigma_{rms} \approx 10$ μm. Measurements of beam mistiming yield $\sigma_{rms} \approx 5$ ps.[42] Beam imbalance, mispointing, and mistiming of such magnitudes as well as the beam overlap perturbations and 10-μm target offset (located in the equatorial plane, as in Model A2) were all included in Model A3.

Model A3 shows moderate reduction of the implosion performance in comparison with Model A2 (see Table 1). This suggests that the 10-μm offset is a dominant source of nonuniformities in both models. Figures 3(b) and 3(d) show the equatorial distributions of ρ and T_i at peak neutron production in Model A3. This model, like Model A2, shows a large-scale ($m = 1$) asymmetry in the stagnated dense shell, in which, however, perturbations with $m \sim 10$ from individual beams are more pro-

nounced than in Model A2 [compare Figs. 3(a) and 3(b)]. The latter could be because of the effects of beam imbalance, mispointing, and mistiming that enhance nonuniformities with ℓ and $m \sim 10$. It is worth noting that the narrow jet in the hot spot seen in Model A2 is "washed out" during interactions with other perturbations in Model A3 and is not as destructive for the integrity of the dense shell as that in Model A2 [compare Figs. 3(a) and 3(b)].

One notes that Model A3 still overperforms the real implosion (see Table 1). It is possible, therefore, that the sources of nonuniformity assumed basing on the indirect measurements underestimate the real sources. To study sensitivity of this implosion design to variation of the sources magnitude and to find the most important sources, Models A4, A5, A6, and A7 were simulated. Each of these models has perturbation σ_{rms} for the each individual source increased by a factor of 2. The results are listed in Table 1.

Models A4–A7 confirm that the target offset is the most destructive factor for the considered implosion. Model A7, which assumes a 20-μm offset, has the lowest neutron yield that is close to the measured one (0.218 and 0.195 in relative units, respectively). The hot spot pressure P_{hs} in Model A7 is reduces by about a factor of 2 with respect to that in the uniform implosion (Model A0) and, again, the simulated pressure quite closely reproduces the pressure inferred from the experiment (see Table 1). A model showing the second worst performance after Model A7 is Model A4, which assumes the beam imbalance σ_{rms} increased to 20%. This model suffers from large-scale (with modes ℓ and m from 1 to ~ 3) distortions of the implosion shell. The simulations have demonstrated that perturbations introduced by increased beam mistiming (Model A6) and mispointing (Model A5) do not have big effects on the implosion performance. It is worth to note that Model A5 demonstrates a little better performance than Model A3 despite of the increased beam mispointing in the former model. This is because the large-scale perturbations introduced in Model A5 because

of mispointing have phases that are opposite to those introduced because of the target offset. As a result, the effects of mispointing somewhat compensate the effects of offset. Such an occasional compensation (or amplification) of low ℓ- and m-modes in the course of interactions of perturbations from different sources is expected.

Figures 4(a) and 4(b) show the equatorial cross-sections of the distributions of ρ and T_i in Model A7 at peak neutron production, $t = 2.57$ ns. The distortion of the stagnated shell because of the 20-μm offset is apparent: the shell mass concentrates on the side that is opposite to the offset (shown by the arrow) and the hot bubble blows out the shell in the direction alone the offset [see Figs. 4(a) and 4(b)]. Figures 4(c) and 4(d) show x-ray and neutron images of Model A7 taken from the polar location. The x-ray image was formed by photons in the energy range from 4 to 8 keV at the same time as in the images in Figs. 4(a) and 4(b). The x-ray image is constructed applying an experimental 30-ps temporal averaging and 6-μm spatial averaging.[11] The neutron image was time-integrated over the whole neutron production history and used a 6-μm spatial averaging. One finds in Fig. 4(c) that dark areas corresponding to high x-ray emissivity loosely represents the shapes of highly distorted dense shell and hot spot: contrary to the case of uniform implosions, in which such dark areas originate in regions of the maximum T_i, these dark areas originate in the regions of large and oppositely directed gradients of ρ and T_i. The black lines in the images in Fig. 4 show a 17% x-ray emissivity contour, which well represents the volume of hot spots with relatively small distortions and is typically used for estimating the hot spot pressure.[43] Model A7 provides an example that such a contour does not include the whole volume of the hot spot missing the volume of the hot bubble penetrating the shell [the feature in the upper right corner in Figs. 4(a) and 4(b)].

The dark (bright) areas in the neutron image of Model A7 [Fig. 4(d)] closely follow the distribution of T_i [Fig. 4(b)] and, therefore, better represent the shape of the hot spot. The discrepancy between the bright areas in the x-ray and neutron images is

explained by the different functional dependency of the corresponding emissivities on plasma parameters. Note that the similar discrepancy between x-ray and neutron images was found in HYDRA simulations of indirect-drive implosions on the NIF.[21]

3. The energy balance

The deceleration stage is characterized by conversion of the majority of the kinetic energy E_{kin} of an implosion shell into the thermal energy E_{th} of a hot spot. This process is illustrated in Fig. 5, which shows the evolution of E_{kin} and E_{th} in Models A0 and A7 (red and blue lines, respectively) representing the extreme cases of the uniform and most perturbed implosions in Table 1. The energies E_{kin} and E_{th} were calculated integrating over the volume of the radius of 200 μm around the grid center. At the time interval displayed in Fig. 5, the implosion shells were well inside this radius in both models. The peak kinetic energy, $\tilde{E}_{kin} = 4.4\%$ (the upper tilde means that the energy is normalized to the laser energy of 26 kJ), is reached at $t = 2.35$ ns in both models. After the peak, the shell decelerates losing this energy. Model A0 shows a fastest reduction of E_{kin} and is characterized by the lowest residual kinetic energy $(\tilde{E}_{kin})_{res} = 0.2\%$, which is reached at stagnation, $t_{st} = 2.59$ ns. The residual kinetic energy in spherically symmetric models is mainly defined by the ratio of shocked and unshocked mass of the stagnated shell and specific to a particular implosion design.[4] At the same time when E_{kin} takes the minimum, E_{th} approaches its maximum, $(\tilde{E}_{th})_{max} = 6.4\%$. After the stagnation, the shell expands converting the accumulated thermal energy back into the kinetic energy.

The simulations of Model A7 show that parts of the perturbed shell continue to move at the time of stagnation, which is to about 10 ps earlier than that in Model A0. These movements increase $(\tilde{E}_{kin})_{res}$ till 1.1% and reduce $(\tilde{E}_{th})_{max}$ till 5.5% (comparing with 0.2% and 6.4% in Model A0, respectively). The reduction of $(\tilde{E}_{th})_{max}$ indicates

an undercompression of the hot spot and explains the apparent reduction of neutron rate in Model A7 (compare the red and blue dashed lines in Fig. 5) The neutron rate peak in Model A7 is about 10 ps earlier than that with Model A0. Rising of the neutron rates in both models occurs at about same time, but the rate decrease after the peak in the case of Model A7 is about 20 ps earlier. This behavior reproduces the experimental "burn truncation." [13]

Figure 5 shows the evolution of the total energy $E_{kin} + E_{th}$ in Models A0 and A7. These energies are almost constant and closely follow each other before, at, and after stagnation in agreement with the expectation of conservation of the total energy. This illustrates a good consistency of the simulations. The fact that $E_{kin} + E_{th}$ are not exactly constant can be explained by a small heat and mass transfer through the boundary of the 200-μm-radius integration volume, which is used to estimate these energies.

4. The hot spot pressure

Figure 6 shows the evolution of the instantaneous neutron averaged pressure in Model A0 (red solid line). This pressure reaches its peak about 5 ps after the neutron rate peak (red dashed line). The peak pressure in Model A7 is reduced by a factor of 2 (blue solid line) and delayed by about 15 ps from the corresponding neutron rate peak (blue dashed line). The increased delay between the peaks in the latter case can be explained by the nonuniformities. The instantaneous neutron averaged pressure taken at the neutron rate peak is related to the hot spot pressure P_{hs} inferred from measurements.[43] Analyzing the delays between the pressure and neutron rate peaks in Models A0 and A7, one concludes that P_{hs} in nonuniform implosions can be reduced because of two reasons: because of undercompression of the hot spot and because of an early-time sampling of the pressure. Table 1 lists P_{hs} in Models A0–A7 and

also the inferred hot spot pressure in shot 78378. It is worth noting good agreement between the latter pressure, 45 ± 6 Gbar, and $P_{hs} = 46.5$ Gbar in Model A7. This agreement as well as good agreement between the measured and simulated neutron yields in Model A7 (in terms of YOU, they are 0.20 and 0.22, respectively) suggest that nonuniformities in shot 78378 can be as large as in Model A7.

5. Hot spot temperature

The hot spot ion temperature T_i in ICF implosions is commonly determined measuring the width of the energy spectrum of the fusion-produced neutrons.[44] The spread of neutron energy arises from the thermal velocities of reacting pair of ions (D and T in our case) and from motions of the reacting plasma, or the bulk motion effect. The latter effect can results in significant differences between T_i inferred from the spectrum and the actual T_i.[29]

Figure 7(a) show example DT neutron spectra that were obtained by post-processing data from Model A7. The post-processor is based on the model of spectra from neutron emitted plasma in Ref. [29]. The black line in Fig. 7(a) presents the spectrum without the bulk motion effect, which corresponds to the neutron averaged $(T_i)_n = 2.73$ keV. The green, blue, and dashed red lines show the spectra with the bulk motion effect assuming that viewing angles were in the directions indicated in Fig. 7(b) by the corresponding color arrows. The spectrum in green is measured in the position of 90° from the target offset (the viewing angle alone the z-axis), and the spectra in blue and red are measured in the positions of 45° (the viewing angles alone the y- and x-axises, respectively). The offset introduces large nonuniformities and a jet-like motion in the hot spot of Model A7 (see Fig. 4). It is not surprising, therefore, that the spectrum width and displacement strongly correlate with the viewing angles. The spectrum at 90° (in green) insignificantly deviates from the the spectrum in black

and the inferred T_i is 2.9 keV, which is close to $(T_i)_n = 2.73$ keV. This is because the motions in the hot spot have small projection components on the corresponding viewing direction. The spectra in blue and red are displaced by about 50 keV with respect to the spectrum in black and have larger widths that inf ere $T_i = 4.6$ and 4.7 keV, respectively. The large difference between the latter temperatures and $(T_i)_n$ is an indication of large bulk velocities in the hot spot. The small deviation between the spectra in blue and red in Fig. 7(a) indicates a small effect of nonuniformities from sources other than the offset.

6. Mount stalk

Mount stalks can source large-scale nonuniformities in direct-drive implosions contributing to the performance degradation.[14] The effect of mount stalk in shot 78378 was simulated assuming surrogate perturbations, which are localized perturbations in the laser deposition that approximately mimic the effect of the stalk. Figure 8(a) shows the equatorial cross-section of the model, which assumes perturbations form the beam overlap and mount stalk. The stalk results in a narrow dense Rayleigh-Taylor spike growing from the inner surface of the decelerating implosion shell. This spike penetrates the hot spot creating a jet-like motion of the hot spot plasma. The nonuniformities form the stalk can interact with nonuniformities from other sources including target offsets, beam imbalance, beam mispointing, and beam mistiming. Figure 8(b) shows Model A6, which include these sources and does not include the effect of the stalk, and Figs. 8(c) and 8(d) show models having same perturbations as Model A6 plus perturbations from the stalk at two different locations indicated by the black arrows. Figure 8(c) presents the case when the stalk has the same location as in Fig. 8(a) forming an angle of 135° with the target offset. Figure 8(d) presents the case when the angle is 45°. Apparently, the stalks in the both cases introduce

minor distortions to the shape of the implosion shell and hot spot.

7. Comparison with flux-limited simulations

Most multi-dimension direct-drive ICF simulations are conducted without CBET and employing the flux-limited heat transport with the flux-limiter $f \sim 0.04$ to 0.06 (the "flux-limited" model). Figure 9 compares two ASTER simulations of shot 78378 using the laser deposition and heat transport models accepted in this paper (the "Spitzer" model, see Section II) and the flux-limited model [Figs. 9(a) and 9(b), respectively]. Both simulations assume perturbations because of the beam overlap and a 20-μm target offset at the equatorial plane. The flux-limited simulations use a time-dependent f, which equals to 0.065 during the pickets and then gradually reduces to 0.04, which is kept during the main drive (see Fig. 1). One can see in Fig. 9 that the shells at the peak neutron production differ substantially by the shape and displacement of the shell's centroids (shown by blue crosses) with respect to the initial shell position (shown by black crosses). Simulations using the Spitzer model demonstrate an about 20-μm displacement, whereas those using the flux-limited model produce only an about 6-μm displacement. The shell also develop much large density nonuniformities in the former case [Fig. 9(a)]. Apparently, the performance degradation is more significant in the case of the more distorted Spitzer model, which results in $YOC = 0.25$ versus 0.85 in the case of the flux-limited model. Flux-limited 2D DRACO simulations of the same 20-μm offset implosion have shown good agreement with the flux-limited ASTER model.

These ASTER simulations suggest that using the flux-limited heat transport in direct-drive ICF simulations can result in an underestimation of laser-imposed nonuniformities. Two explanations of this phenomenon can be proposed. The first one is that the radial inward heat flux limited at the critical radius becomes less sensitive

to variations of the heat sourcing by the laser absorption. The second explanation considers enhancing lateral heat fluxes in the hot corona outside the critical radius because of increasing the electron temperature. The flux limitation reduces cooling of the corona and, therefore, can increase the temperature. Other reason of increasing the temperature is the absence of CBET, which otherwise shifts the energy deposition region from the critical away to approximately quarter-critical radius.[9] To test the latter explanation, a flux-limited ASTER simulation of shot 78378 were performed, in which the lateral heat fluxes were turned off. The simulation shows an about 12-μm displacement of the implosion shell centroid, which is in between the displacements found in the Spitzer (20 μm) and flux-limited (6 μm) models. The letter test suggests that the both proposed explanations are likely valid.

B. High-performance R75 design

The R75 design employs reduced laser beams ($R_b/R_t = 0.75$) for the purpose of mitigating CBET losses. As a result of this mitigation, the hydrodynamic efficiency of the design is increased reaching $\tilde{E}_{kin} = 5.7\%$ [versus 4.4% in the case of the nominal design (see Fig. 5)]. To benefit form this increase, the R75 design has a larger-diameter and heavier target while keeping the same laser energy of 26 kJ. The target structure and laser pulse of the R75 design is shown in Fig.1(b). The target consists of a 70-μm thick DT-ice shell overcoated with a 8-μm thick and 450-μm outer radius plastic (CD) shell. The laser pulse is similar to that used in shot 78378 and only slightly modified to accommodate to the different target dimensions. The 1D neutron yield in this design is 4.12×10^{14}, which is about a factor of 2 larger than that in shot 78378. Selected simulations of the R75 design, including uniform Model B0, are listed in Table 2.

The increased hydrodynamic efficiency results in the larger convergence ratio (the

ratio of the initial target radius to the minimum one estimating in 1D simulations), which is 18.5 in the case of the R75 design and 16.5 in the case of the nominal design. The larger ratio in the former case can lead to some enhancement of the low- and middle-wavelength perturbation modes ($\ell \lesssim 50$) causing by the secular and Bell-Plesset[45] growths.

1. Beam overlap perturbations

The reduction of the laser beam size results in enhancing nonuniformities in implosion shells because of beam overlap perturbations. Figure 10 presents simulations of the R75 design, which assume such perturbations and assume a supergaussian beam profile with the index $N_{SG} = 5$. This figure shows the distributions of ρ and T_i in the equatorial [Figs. 10(a) and 10(c), respectively] and meridional [Figs. 10(b) and 10(d), respectively] cross-sections of the implosion target at the peak neutron production, $t = 2.94$ ns. Distortions of the dense shell with the dominant ℓ- and m-modes equal to 10, which are seeded by beam overlapping, are apparent. Large density spikes seen Figs. 10(a) and 10(b) develop because of the Rayleigh-Taylor growth. The distribution of T_i [Figs. 10(c) and 10(d)] clearly show hot Rayleigh-Taylor bubbles, which move through the decelerated shell outward. These perturbations should be compared with the perturbations in shot 78378 produced by the beam-ports, but at different illumination conditions (see Fig. 2). The beam overlap perturbations in the R75 design result in $YOC = 0.75$ (Model B1, see Table 2) and reduction of P_{hs} form 140 Gbar in the case of the 1D implosion (Model B0) to 132 Gbar.

Perturbations from beam overlap depend on the index N_{SG}. This was demonstrated considering illumination patterns created by laser beams on a solid sphere.[46] Refraction of laser light in the corona of implosion targets can change the illuminations/absorption pattern and make it time-dependent.[47] ASTER simulations take

into account these effects. Figure 11 shows the simulated neutron yield as a function of N_{SG} (solid line). One sees that the variation of N_{SG} within the range from 2 to 5 (the values $\gtrsim 5$ are not practical because of manufacturing limitations of the beam forming optics) can cause a factor of about 2 variation of the neutron yield. There is a sharp peak in the neutron yield at $N_{SG} = 2.42$ and a flat minimum at $N_{SG} \approx 3.6$. The neutron yield gradually increases from this minimum while increasing N_{SG} to 5.

The improvements in the neutron yield near $N_{SG} = 2.42$ is because of improvements of implosion uniformity caused by a change of the phase of the dominant $\ell = 10$-mode. Figure 12 shows implosion shells at the peak neutron production for four different values of $N_{SG} = 2.3$, 2.42, 3.4, and 5, which are indicated in Fig. 11 by the solid circles. The shell with $N_{SG} = 2.42$ [Fig. 12(b)] shows minimum $\ell = 10$ perturbations and corresponds to the maximum performing implosion. The largest nonuniformities present in the shell with $N_{SG} = 3.4$ [Fig. 12(c)], which produces the minimum neutron yield. The shell with $N_{SG} = 2.3$ demonstrates an inversion of the phases of the nonuniformity modes in comparison with the cases of $N_{SG} = 3.4$ and 5. This inversion is observed as exchanging the positions of the bubbles and spikes in Fig. 12(a) ($N_{SG} = 2.3$) and in Figs. 12(c) and 12(d) ($N_{SG} = 3.4$ and 5, respectively).

The results of simulations assuming only the beam overlap perturbations suggest that the best beam shape to be chosen for implosion experiments can be the one with $N_{SG} = 2.42$. This, however, is not confirmed by simulations with additional sources of nonuniformities. These sources are assumed to be the same as those considered in the case of the nominal design and have a 10-μm target offset, 10% σ_{rms} beam imbalance, 10-μm σ_{rms} beam mispointing, and 5-ps σ_{rms} beam mistiming. The dependence of the neutron yield on N_{SG} for these simulations are shown in Fig. 11 by the dashed line. The neutron yield in the whole range of N_{SG} reduces because of the additional perturbations and the variation of the yield is also reduced. The peak at $N_{SG} = 2.42$ still exists, but becomes much wider, and its value is a little less than the neutron

yield at $N_{SG} = 5$. Figures 13 and 14 compare the distributions of ρ and T_i at the peak neutron production for the cases of $N_{SG} = 2.42$ and 5, respectively. The presence of Rayleigh-Taylor density spikes and hot bubbles, which sizes are similar in the both cases, is evident. These simulations suggest that beams with $N_{SG} \approx 2.4$ and 5 can both be used in implosion experiments expecting that they both will show similar performance. All further simulations of the R75 design will assume $N_{SG} = 5$.

2. Perturbations from target offset

Figures 15 illustrates the effect of target offsets in the R75 design, showing the equatorial cross-sections of the implosion shells with the offsets of 5, 10, 15, and 20 μm [Figs. 15(a), 15(b), 15(c), and 15(d), respectively]. The shells are shown at the peak neutron production, $t \approx 2.93$ ns, and their offsets were assumed in the equatorial plane. These simulations have no other sources of nonuniformities accept the one because of the beam overlap.

The offsets result in jet-like flows in the hot spot, which interact with the Rayleigh-Taylor spikes and bubbles produced by the beam overlap perturbations. The flows enhance the growth of the bubbles in the direction of the offset and result in blowing out the shells in the case of the offsets of 10 μm and larger. The dependencies of the YOC and hot spot pressure P_{hs} on the offsets are shown by the solid squares in Figs. 16 and 17, respectively. The solid circle in Fig. 17 shows $P_{hs} = 140$ Gbar corresponding to uniform Model B0. The implosion performance quickly degrades with increasing the offset. The neutron yield reduces by a factor of 2 for the offset of 10 μm (compare Models B1 and B2) and by a factor of 5 to 6 for the offset of 20 μm. The pressure P_{hs} reduces from 132 Gbar in the case of the zero offset (Model B1) to 95 and 53 Gbar in the case of the offsets of 10 (Model B2) and 20 μm, respectively.

3. Perturbations from all sources

The solid triangles in Figs. 16 and 17 illustrate the changes of YOC and P_{hs} when sources of nonuniformities because of the beam imbalance (10% σ_{rms}), mispointing (10 μm σ_{rms}), and mistiming (5 ps σ_{rms}) were added in the simulations with the offsets. It is worth noting that the effects of these perturbations on the implosion performance are roughly equivalent to adding a 7-μm offset to the target with the drive assuming only the beam overlap perturbations. The solid- and dashed-lines in Figs. 16 and 17 converge for large offsets indicating that the relative effect of the perturbations because of beam imbalance, mispointing, and mistiming reduces with increasing the offset.

Table 2 lists Models B3-B7, which illustrates the sensitivity of the R75 design to variation of the sources of nonuniformities. Model B3 represents implosions with the same sources as those used in Model A3 of the nominal design (see Table 1). Models B4, B5, and B6 assume a consequent increase by a factor of 2 of σ_{rms} for the beam imbalance, mispointing, and mistiming, respectively. Model B7 has a twice larger target offset, 20 μm. One sees from Table 2 that the latter model demonstrates the worst performance: YOC reduces to 0.097, $(T_i)_n$ reduces from 3.61 keV (Model B0) to 2.64 keV, and P_{hs} is only 48 Gbar, which is about a factor of 3 less than that in Model B0. The second worst performing model is Model B4, which assumes a 20% beam imbalance. The numbers here are $YOC = 0.146$, $(T_i)_n = 2.9$ keV, and $P_{hs} = 61$ Gbar. The performance of Models B5 (with a 20-μm beam mispointing) and Model B6 (with a 10-ps beam mistiming) insignificantly deviate from that of Model B3 (see Table 2). YOC and P_{hs} for Models B4, B5, and B6 are shown in Figs. 16 and 17 by the open triangles, circles, and diamonds, respectively. In conclusion, similar to the case of the nominal design (see Section II), one finds that the most important sources of performance degradation in the R75 design are the target offset and beam imbalance.

IV. DISCUSSION AND CONCLUSIONS

Cryogenic implosions on the OMEGA laser system can suffer from large-scale ($\ell \lesssim 10$) laser imposed nonuniformities. Sources of these nonuniformities include perturbations caused by target offsets and beam overlap, imbalance, mispointing, and mistiming. Typical magnitudes of the beam imbalance, mispointing, and mistiming perturbations suggesting by indirect measurements are (in terms of σ_{rms}): 10%, 10 μm, and 5 ps, respectively. The target offsets are typically measured from about 10 to 20 μm. A development of large-scale nonuniformities imposed by these sources in two cryogenic mid-adiabat ($\alpha = 4$) implosion designs (see Fig. 1) was studied using the 3D ICF code ASTER.

Simulations of the nominal design (OMEGA shot 78378), which has $R_b/R_t \approx 1$, have demonstrated insignificant roles of perturbations produced by beam overlap, mispointing, and mistiming (see Table 1). The largest reduction of the implosion performance was found because of target offsets of 10 μm and more. The offsets result in a significant distortion of the stagnated implosion shell with the dominant $\ell = 1$ perturbation mode (see Fig. 4). Asymmetric motions in the hot spot of such offset targets cause substantial broadening of neutron spectra, which are measured in directions roughly aligned with the direction of the offset. The hot spot ion temperature inferred from these spectra can be up to about a factor 2 larger than the actual neutron averaged ion temperature (Fig. 7). The distorted implosions remain undercompressed with the hot spot thermal energy up to about 20% lower than the energy in the corresponding 1D implosion (Fig. 5). Such undercompression in Model A7 (see Table 1) results in a factor of 5 reduction of the neutron yield and a factor of 2 reduction of the hot spot pressure. The implosion performance demonstrated by Model A7 with respect to the neutron yield, hot spot pressure, and maximum inferred ion temperature is in good agreement with measured performance of shot 78378 (see

Table 1).

Perturbations from beam imbalance introduce nonuniformities in implosion shells with the dominant ℓ-modes from 1 to $\sim$ 3. These perturbations begin to compete with perturbations produced by a 10-μm target offset when the imbalance magnitude (in terms of σ_{rms}) is larger than 10%.

Simulated x-ray images (in the photon energy range from 4 to 8 keV) of hot cores of highly distorted nominal design implosions demonstrate that these images can loosely reproduce the shape of the cores [see Figs. 4(b) and 4(c)]. This is because the maximum x-ray emission comes from regions with large and oppositely directed gradients of the electron temperature and density. These regions locate near dense parts of distorted shells and do not coincide with the maximum temperature regions representing the hot spot. Better agreements demonstrate simulated neutron images, which well represent the shape of the core's hot region [see Fig. 4(d)].

Simulations of the effects of the mount stalk in shot 78378 were conducted assuming surrogate perturbations in the laser deposition. These effects are predicted to be relatively small in comparison with other dominant sources of nonuniformities (see Fig. 8).

Test simulations of shot 78378 have revealed that the flux-limited heat transport (with the flux-limiter $f \sim 0.04$ – 0.06) can result in a substantial underestimation of the laser-imposed nonuniformities in implosion targets. Figure 9 shows differences between the distortion and displacement of the stagnated implosion shells caused by a 20-μm target offset in two cases of the full Spitzer and flux-limited simulations. The displacement of the shell centroid is about 20 μm in the former case and only about 6 μm in the latter case. This example illustrates the drive symmetry change depending on the used model of the heat transport. There are two possible mechanisms explaining this difference. Firstly, the flux-limitation reduces the response of the inward heat flux to variations of the deposited laser energy. Secondly, the flux-limitation

and absence of CBET (which is not included in flux-limited simulations) increase the temperature of the corona outside the critical radius. The latter increase results in increasing lateral heat fluxes, which reduce the coronal temperature variations around targets caused by the nonuniform laser deposition.

Considering the large difference found in implosion simulations using the full Spitzer and flux-limited heat transport models, it is important to determine which the model is more appropriate. It should be mentioned that historically, the flux-limited heat transport was introduced as a simple fix in 1D simulations, which allows to limit laser drive and fit key results of ICF implosion experiments (e.g., the bang time and absorbed laser energy) using a single parameter, the flux-limiter f. Therefore, this model does not have a physical basement. There are also no physical motivations in application of this model to multi-dimension simulations. Contrary, the Spitzer model is physically well motivated for single and multi-dimension applications and well describes various direct-drive ICF implosion experiments when CBET is included in simulations (see Section II for more discussions). Under this circumstance, one can concludes that the Spitzer model (with CBET) is more appropriate for modeling multi-dimension implosions and one should use caution when applying the flux-limited model in such simulations.

The R75 design, which is characterized by $R_b/R_t = 0.75$, demonstrates better 1D performance in comparison the the nominal design, but suffers more from nonuniformities developed because of beam overlap and other laser-imposed perturbations. The beam overlap nonuniformities depend on the supergaussian index N_{SG} of the beam profile (see the solid line in Fig. 11). There is a "sweet spot", $N_{SG} = 2.42$, which corresponds to the minimum nonuniformities and maximum neutron yield that result from changing the phases of the dominant perturbations with the mode $\ell = 10$ (see Fig. 12). This dependence on N_{SG} is changed when other sources of nonuniformities because of target offset, beam imbalance, beam mispointing, and beam mistiming

were added in simulations (see the dashed line in Fig. 11). The implosions with all these sources demonstrate similar implosion performance in the case of $N_{SG} \approx 2.4$ and 5 (while the latter one demonstrates a little better performance), and about 20% neutron yield deep for N_{SG} between these two.

The target offset in the R75 design has the largest effect over other sources of nonuniformities, like that was found in the case of the nominal design. Changes of the shape of the stagnated implosion shells and changes of the implosion performance depending on the offset are illustrated in Figs. 15, 16, and 17. Perturbations because of beam overlap help the hot bubbles caused by the offset to grow faster (see Fig. 15). The neutron yield is reduced by a factor of about 2 in simulations assuming beam overlap perturbations and target offsets when the offset changes from zero to 10 μm (Fig. 16, the solid line) and the hot spot pressure does it when the offset goes from zero to 15 μm (Fig. 17, the solid line). Adding other sources of nonuniformities (beam imbalance, mispointing, and mistiming) somewhat reduces both the neutron yield and hot spot pressure, but does not change the mentioned reduction trend (Figs. 16 and 17, the dashed lines).

Studding the sensitivity of the nominal and R75 designs to various source of nonuniformities yields the same conclusion: the performance of cryogenic OMEGA designs is most sensitive to target offset and beam imbalance variations (see Table 1, Models A4 and A7, and Table 2, Models B4 and B7). This suggests, therefore, that future improvements of the performance of cryogenic OMEGA implosions should be based mainly on efforts to reduce these two sources.

Comparison of simulations of the nominal and R75 designs have shown that the latter design demonstrate definitely better performance when perturbations because of only beam overlap are considered. The R75 design yields 3.1×10^{14} neutrons (Model B1) versus 2.3×10^{14} neutrons in the case of the nominal design (Model A1) and the hot spot pressures are 132 and 94 Gbar, respectively. Addition of other

nonuniformities results in a relatively sharp degradation of the neutron yield in the R75 design, so that the latter predicts about the same yields in Models B2-B7 as those in Models A2-A7 of the nominal design having the same sources of nonuniformities, respectively (e.g., 4.0×10^{13} in Model B7 and 4.6×10^{13} in Model A7). The relative degradation of the hot spot pressure in the R75 design, when adding nonuniformities, is more gradual: this pressure is predicted to be always larger in the R75 design than in the nominal design having the same sources (compare Models B2-B7 and Models A2-A7, respectively). Note that the hot spot pressures in highly perturbed models of the R75 design (Models B4 and B7) just marginally exceed those of the nominal design (Models A4 and A7).

In summary, implosions of the R75 design are expected to perform similarly to those of the nominal design in the case of the current laser-imposed nonuniformities on OMEGA, e.g., like in Models A7 and B7. Simulations predict that the R75 design could demonstrate performance advantages, exceeding the 1D performance of the nominal design and achieving the 100-Gbar pressure goal, in the case of the target offsets $\lesssim 5$ μm and beam imbalance $\sigma_{rms} \lesssim 5\%$. The current beam mispointing ($\sigma_{rms} \sim 10\%$) and mistiming ($\sigma_{rms} \sim 5$ ps) on OMEGA are sufficient.

ACKNOWLEDGMENT

This material is based upon work supported by the Department of Energy National Nuclear Security Administration under Award Number DE-NA0001944, the University of Rochester, and the New York State Energy Research and Development Authority. The support of DOE does not constitute an endorsement by DOE of the views expressed in this article.

APPENDIX A: CALCULATION OF MATERIAL FRACTIONAL VOLUME

The fractional volume $f^\alpha = V^\alpha/V$ is calculated assuming the ideal gas model for ionized plasma in the thermal and dynamic equilibrium. Here $V = \sum_\alpha V^\alpha$ is the volume of a numerical cell and V^α is the volume in the cell occupied by the material α. The total pressure in the cell is given by

$$P = \sum_\alpha (Z^\alpha + 1) n_{\rm i}^\alpha T \tag{17}$$

where T is the temperature in the energy unit. This pressure should be equal to the pressure of the material α concluded in the volume V^α,

$$P = (Z^\alpha + 1) \frac{n_{\rm i}^\alpha}{f^\alpha} T. \tag{18}$$

Equating the right hand sides of eqs. (17) and (18), one gets,

$$f^\alpha = \frac{(Z^\alpha + 1) n_{\rm i}^\alpha}{\sum_\alpha (Z^\alpha + 1) n_{\rm i}^\alpha}. \tag{19}$$

Equation (19) assumes that $T_i = T_e = T$. In the more general case of $T_i \neq T_e$, one gets

$$f^\alpha = \frac{(Z^\alpha T_e + T_i) n_{\rm i}^\alpha}{\sum_\alpha (Z^\alpha T_e + T_i) n_{\rm i}^\alpha}. \tag{20}$$

APPENDIX B: COORDINATES OF OMEGA BEAM-PORTS

The location of the 60 OMEGA beam-ports around the OMEGA target chamber center are presented in the spherical coordinates, which are arranged in two tables for the angles θ and ϕ, respectively.

θ (degree)				
21.415	21.415	21.415	21.415	21.415
42.020	42.020	42.020	42.020	42.020
58.852	58.852	58.852	58.852	58.852
58.852	58.852	58.852	58.852	58.852
81.240	81.240	81.240	81.240	81.240
81.240	81.240	81.240	81.240	81.240
98.760	98.760	98.760	98.760	98.760
98.760	98.760	98.760	98.760	98.760
121.148	121.148	121.148	121.148	121.148
121.148	121.148	121.148	121.148	121.148
137.980	137.980	137.980	137.980	137.980
158.585	158.585	158.585	158.585	158.585

ϕ (degree)				
54.000	126.000	198.000	270.000	342.000
54.000	126.000	198.000	270.000	342.000
5.938	30.062	77.938	102.062	149.938
174.062	221.938	246.062	293.938	318.062
41.459	66.541	113.459	138.541	185.459
210.541	257.459	282.541	329.459	354.541
174.541	149.459	102.541	77.459	30.541
5.459	318.541	293.459	246.541	221.459
138.062	113.938	66.062	41.938	354.062
329.938	282.062	257.938	210.062	185.938
162.000	90.000	18.000	306.000	234.000
162.000	90.000	18.000	306.000	234.000

References

[1] T. R. Boehly, D. L. Brown, R. S. Craxton, R. L. Keck, J. P. Knauer, J. H. Kelly, T. J. Kessler, S. A. Kumpan, S. J. Loucks, S. A. Letzring, i F. J. Marshall, R. L. McCrory, S. F. B. Morse, W. Seka, J. M. Soures, C. P. Verdon, Opt. Commun. **133**, 495 (1997).

[2] S. Atzeni and J. Meyer-ter-Vehn, *The Physics of Inertial Fusion: Beam Plasma Interaction, Hydrodynamics, Hot Dense Matter*, International Series of Monographs on Physics (Clarendon, Oxford, 2004), pp. 4750.

[3] J.D. Lindl, *Inertial Confinement Fusion* (Springer, New York, 1998), pp. 39, 61.

[4] V. N. Goncharov, T. C. Sangster, R. Betti, T. R. Boehly, M. J. Bonino, T. J. B. Collins, R. S. Craxton, J. A. Delettrez, D. H. Edgell, R. Epstein, R. K. Follett, C. J. Forrest, D. H. Froula, V. Yu. Glebov, D. R. Harding, R. J. Henchen, S. X. Hu, I. V. Igumenshchev, R. Janezic, J. H. Kelly, T. J. Kessler, T. Z. Kosc, S. J. Loucks, J. A. Marozas, F. J. Marshall, A. V. Maximov, R. L. McCrory, P. W. McKenty, D. D. Meyerhofer, D. T. Michel, J. F. Myatt, R. Nora, P. B. Radha, S. P. Regan, W. Seka, W. T. Shmayda, R. W. Short, A. Shvydky, S. Skupsky, C. Stoeckl, B. Yaakobi, J. A. Frenje, M. Gatu-Johnson, R. D. Petrasso, and D. T. Casey, Phys. Plasmas **21**, 056315 (2014).

[5] W. Seka, D. H. Edgell, J. P. Knauer, J. F. Myatt, A. V. Maximov, R. W. Short, T. C. Sangster, C. Stoeckl, R. E. Bahr, R. S. Craxton, J. A. Delettrez, V. N. Goncharov, I. V. Igumenshchev, and D. Shvarts, Phys. Plasmas **15**, 056312 (2008).

[6] D. T. Michel, C. Sorce, R. Epstein, N. Whiting, I. V. Igumenshchev, R. Jungquist, and D. H. Froula, Rev. Sci. Instrum. **83**, 10E530 (2012).

[7] J, Delettrez, R. Epstein, M. C. Richardson, P. A. Jaanimagi, and B. L. Henke, Phys. Rev. A **36**, 3926 (1987).

[8] V. N. Goncharov, T. C. Sangster, P. B. Radha, R. Betti, T. R. Boehly, T. J. B. Collins, R. S. Craxton, J. A. Delettrez, R. Epstein, V. Yu. Glebov, S. X. Hu, I. V. Igumenshchev, J. P. Knauer, S. J. Loucks, J. A. Marozas, F. J. Marshall, R. L. McCrory, P. W. McKenty, D. D. Meyerhofer, S. P. Regan, W. Seka, S. Skupsky, V. A. Smalyuk, J. M. Soures, C. Stoeckl, D. Shvarts, J. A. Frenje, R. D. Petrasso, C. K. Li, F. Séguin, W. Manheimer, and D. G. Colombant, Phys. Plasmas **15**, 056310 (2008).

[9] I. V. Igumenshchev, D. H. Edgell, V. N. Goncharov, J. A. Delettrez, A. V. Maximov, J. F. Myatt, W. Seka, A. Shvydky, S. Skupsky, and C. Stoeckl, Phys. Plasmas **17**, 122708 (2010).

[10] L. Rayleigh, Proc. London Math Soc. **XIV**, 170 (1883); G. Taylor, Proc. R. Soc. London, Ser. A **201**, 192 (1950).

[11] F. J. Marshall and J. A. Oertel, Rev. Sci. Instrum. **68**, 735 (1997).

[12] C. Forrest, P. B. Radha, V. Yu. Glebov, V. N. Goncharov, J. P. Knauer, A. Pruyne, M. Romanofsky, T. C. Sangster, M. J. Shoup III, C. Stoeckl, D. T. Casey, M. Gatu-Johnson, and S. Gardner, Rev. Sci. Instrum. **83**, 10D919 (2012).

[13] P. B. Radha, V. N. Goncharov, T. J. B. Collins, J. A. Delettrez, Y. Elbaz, V. Yu. Glebov, R. L. Keck, D. E. Keller, J. P. Knauer, J. A. Marozas, F. J. Marshall, P. W. McKenty, D. D. Meyerhofer, S. P. Regan, T. C. Sangster, D. Shvarts, S. Skupsky, Y. Srebro, R. P. J. Town, and C. Stoeckl, Phys. Plasmas **12**, 032702 (2005).

[14] I. V. Igumenshchev, F. J. Marshall, J. A. Marozas, V. A. Smalyuk, R. Epstein, V.

N. Goncharov, T. J. B. Collins, T. C. Sangster, and S. Skupsky, Phys. Plasmas **16**, 082701 (2009).

[15] S. X. Hu, P. B. Radha, J. A. Marozas, R. Betti, T. J. B. Collins, R. S. Craxton, J. A. Delettrez, D. H. Edgell, R. Epstein, V. N. Goncharov, I. V. Igumenshchev, F. J. Marshall, R. L. McCrory, D. D. Meyerhofer, S. P. Regan, T. C. Sangster, S. Skupsky, V. A. Smalyuk, Y. Elbaz, and D. Shvarts, Phys. Plasmas **16**, 112706 (2009).

[16] M. M. Marinak, R. E. Tipton, O. L. Landen, T. J. Murphy, P. Amendt, S. W. Haan, S. P. Hatchett, C. J. Keane, R. McEachern, and R. Wallace, Phys. Plasmas **3**, 2070 (1996); M. M. Marinak, S. W. Haan, T. R. Dittrich, R. E. Tipton, and G. B. Zimmerman, Phys. Plasmas **5**, 1125 (1998); M. M. Marinak, G. D. Kerbel, N. A. Gentile, O. Jones, D. Munro, S. Pollaine, T. R. Dittrich, and S. W. Haan, Phys. Plasmas **8**, 2275 (2001).

[17] E. I. Moses, R. N. Boyd, B. A. Remington, C. J. Keane, and R. Al-Ayat, Phys. Plasmas **16**, 041006 (2009).

[18] D. S. Clark, M. M. Marinak, C. R. Weber, D. C. Eder, S. W. Haan, B. A. Hammel, D. E. Hinkel, O. S. Jones, J. L. Milovich, P. K. Patel, H. F. Robey, J. D. Salmonson, S. M. Sepke, and C. A. Thomas, Phys. Plasmas **22**, 022703 (2015).

[19] C. R. Weber, D. S. Clark, A. W. Cook, D. C. Eder, S. W. Haan, B. A. Hammel, D. E. Hinkel, O. S. Jones, M. M. Marinak, J. L. Milovich, P. K. Patel, H. F. Robey, J. D. Salmonson, S. M. Sepke, and C. A. Thomas, Phys. Plasmas **22**, 032702 (2015).

[20] Brian K. Spears, M. J. Edwards, S. Hatchett, J. Kilkenny, J. Knauer, A. Kritcher, J. Lindl, D. Munro, P. Patel, H. F. Robey, and R. P. J. Town, Phys. Plasmas **21**, 042702 (2014).

[21] Brian K. Spears, David H. Munro, Scott Sepke, Joseph Caggiano, Daniel Clark, Robert Hatarik, Andrea Kritcher, Daniel Sayre, Charles Yeamans, James Knauer, Terry Hilsabeck, and Joe Kilkenny, Phys. Plasmas **22**, 056317 (2015).

[22] S. Skupsky, J. A. Marozas, R. S. Craxton, R. Betti, T. J. B. Collins, J. A. Delettrez, V. N. Goncharov, P. W. McKenty, P. B. Radha, T. R. Boehly, J. P. Knauer, F. J. Marshall, D. R. Harding, J. D. Kilkenny, D. D. Meyerhofer, T. C. Sangster, and R. L. McCrory, Phys. Plasmas **11**, 2763 (2004).

[23] Mark J. Schmitt, Paul A. Bradley, James A. Cobble, James R. Fincke, Peter Hakel, Scott C. Hsu, Natalia S. Krasheninnikova, George A. Kyrala, Glenn R. Magelssen, David S. Montgomery, Thomas J. Murphy, Kimberly A. Obrey, Rahul C. Shah, Ian L. Tregillis, Jessica A. Baumgaertel, Frederick J. Wysocki, Steven H. Batha, R. Stephen Craxton, Patrick W. McKenty, Paul Fitzsimmons, Abbas Nikroo, and Russell Wallace, Phys. Plasmas **20**, 056310 (2013).

[24] Natalia S. Krasheninnikova, James A. Cobble, Thomas J. Murphy, Ian L. Tregillis, Paul A. Bradley, Peter Hakel, Scott C. Hsu, George A. Kyrala, Kimberly A. Obrey, Mark J. Schmitt, Jessica A. Baumgaertel, and Steven H. Batha, Phys. Plasmas **21**, 042703 (2014).

[25] P. B. Radha, F. J. Marshall, J. A. Marozas, A. Shvydky, I. Gabalski, T. R. Boehly, T. J. B. Collins, R. S. Craxton, D. H. Edgell, R. Epstein, J. A. Frenje, D. H. Froula, V. N. Goncharov, M. Hohenberger, R. L. McCrory, P. W. McKenty, D. D. Meyerhofer, R. D. Petrasso, T. C. Sangster, and S. Skupsky, Phys. Plasmas **20**, 056306 (2013).

[26] I. V. Igumenshchev, W. Seka, D. H. Edgell, D. T. Michel, D. H. Froula, V. N. Goncharov, R. S. Craxton, L. Divol, R. Epstein, R. Follett, J. H. Kelly, T. Z. Kosc, A. V. Maximov, R. L. McCrory, D. D. Meyerhofer, P. Michel, J. F. Myatt, T.

C. Sangster, A. Shvydky, S. Skupsky, and C. Stoeckl, Phys. Plasmas **19**, 056314 (2012).

[27] S. X. Hu, V. N. Goncharov, P. B. Radha, J. A. Marozas, S. Skupsky, T. R. Boehly, T. C. Sangster, D. D. Meyerhofer, and R. L. McCrory, Phys. Plasmas **17**, 102706 (2010).

[28] I. V. Igumenshchev, V. N. Goncharov, W. T. Shmayda, D. R. Harding, T. C. Sangster, and D. D. Meyerhofer, Phys. Plasmas **20**, 082703 (2013).

[29] T. J. Murphy, Phys. Plasmas **21**, 072701 (2014).

[30] P. Colella, and P. R. Woodward, J. Comp. Phys. **54**, 174 (1984).

[31] E. F. Toro, *Riemann Solvers and Numerical Methods for Fluid Dynamics* (Springer, Berlin, 1999), p. 115.

[32] P. Colella, and H. M. Glaz, J. Comp. Phys. **59**, 264 (1985).

[33] R. Courant, K. Friedrichs, H. Lewy, "Über die partiellen Differenzengleichungen der mathematischen Physik," Mathematische Annalen **100**, 32 (1928).

[34] S. Braginskii, in *Reviews of Plasma Physics*, edited by M. A. Leontovich (Consultant Bureau, New York, 1965), Vol. 1, p. 205.

[35] L. Spitzer and R. Härm, Phys. Rev. **89**, 977 (1953).

[36] R. C. Malone, R. L. McCrory, R. L. Morse, Phys. Rev. Lett. **34**, 721 (1975).

[37] V. N. Goncharov, T. C. Sangster, T. R. Boehly, S. X. Hu, I. V. Igumenshchev, F. J. Marshall, R. L. McCrory, D. D. Meyerhofer, P. B. Radha, W. Seka, S. Skupsky, C. Stoeckl, D. T. Casey, J. A. Frenje, and R. D. Petrasso, Phys. Rev. Lett. **104**, 165001 (2010).

[38] P. B. Radha, C. Stoeckl, V. N. Goncharov, J. A. Delettrez, D. H. Edgell, J. A. Frenje, I. V. Igumenshchev, J. P. Knauer, J. A. Marozas, R. L. McCrory, D. D. Meyerhofer, R. D. Petrasso, S. P. Regan, T. C. Sangster, W. Seka, and S. Skupsky, Phys. Plasmas **18**, 012705 (2011).

[39] T. R. Boehly, V. A. Smalyuk, D. D. Meyerhofer, J. P. Knauer, D. K. Bradley, R. S. Craxton, M. J. Guardalben, S. Skupsky, and T. J. Kessler, J. Appl. Phys. **85**, 3444 (1999).

[40] S. Skupsky, R. S. Craxton, Phys. Plasmas **6**, 2157 (1999).

[41] R. A. Forties and F. J. Marshall, Rev. Sci. Instrum. **76**, 073505 (2005).

[42] Mistiming

[43] R. Epstein, V. N. Goncharov, F. J. Marshall, R. Betti, R. Nora, A. R. Christopherson, I. E. Golovkin, and J. J. MacFarlane, Phys. Plasmas **22**, 022707 (2015).

[44] M. Gatu Johnson, J. A. Frenje, D. T. Casey, C. K. Li, F. H. Séguin, R. Petrasso, R. Ashabranner, R. M. Bionta, D. L. Bleuel, E. J. Bond, J. A. Caggiano, A. Carpenter, C. J. Cerjan, T. J. Clancy, T. Dppner, M. J. Eckart, M. J. Edwards, S. Friedrich, S. H. Glenzer, S. W. Haan, E. P. Hartouni, R. Hatarik, S. P. Hatchett, O. S. Jones, G. Kyrala, S. Le Pape, R. A. Lerche, O. L. Landen, T. Ma, A. J. MacKinnon, M. A. McKernan, M. J. Moran, E. Moses, D. H. Munro, J. McNaney, H. S. Park, J. Ralph, B. Remington, J. R. Rygg, S. M. Sepke, V. Smalyuk, B. Spears, P. T. Springer, C. B. Yeamans, M. Farrell, D. Jasion, J. D. Kilkenny, A. Nikroo, R. Paguio, J. P. Knauer, V. Y. Glebov, T. C. Sangster, R. Betti, C. Stoeckl, J. Magoon, M. J. Shoup III, G. P. Grim, J. Kline, G. L. Morgan, T. J. Murphy, R. J. Leeper, C. L. Ruiz, G. W. Cooper, and A. J. Nelson, Rev. Sci. Instrum. 83, 10D308 (2012).

[45] G.I. Bell, Los Alamos National Laboratory, Report LA-1321 (1951); M. S. Plesset, J. Appl. Phys. 25, 96 (1954).

[46] B. Canaud, X. Fortin, N. Dague, and J. L. Bocher, Phys. Plasmas **9**, 4252 (2002).

[47] Y. Xu, S. Z. Wu, and W. D. Zheng, Phys. Plasmas **22**, 042708 (2015).

Table 1. Simulated and measured performance of OMEGA shot 78378.

Model	Imbalance (%)	Mispointing (μm)	Mistiming (ps)	Offset (μm)	YOU	P_n (Gbar)	$(T_i)_n$ (keV)
A0[a]	-	-	-	-	1.0	93.8	3.41
A1[b]	-	-	-	-	0.99	93.8	3.41
A2[b]	-	-	-	10	0.611	77.9	3.18
A3[b]	10	10	5	10	0.509	71.0	3.11
A4[b]	**20**	10	5	10	0.364	60.2	2.99
A5[b]	10	**20**	5	10	0.549	73.9	3.19
A6[b]	10	10	**10**	10	0.460	67.1	3.07
A7[b]	10	10	5	**20**	0.218	46.5	2.73
Exp.	~ 10	~ 10	~ 5	$\lesssim 20$	0.20	45 ± 6	3.6/3.7/4.6 $\pm$0.5

[a] Uniform model.

[b] Include beam overlap.

Table 2. Simulated performance of the R75 design.

Model	Imbalance (%)	Mispointing (μm)	Mistiming (ps)	Offset (μm)	YOU	P_n (Gbar)	$(T_i)_n$ (keV)
B0[a]	-	-	-	-	1.0	140.1	3.61
B1[b]	-	-	-	-	0.75	132.3	3.58
B2[b]	-	-	-	10	0.354	94.7	3.22
B3[b]	10	10	5	10	0.240	78.7	3.07
B4[b]	**20**	10	5	10	0.146	61.3	2.90
B5[b]	10	**20**	5	10	0.244	81.4	3.07
B6[b]	10	10	**10**	10	0.215	72.9	3.02
B7[b]	10	10	5	**20**	0.097	48.3	2.64

[a] Uniform model.

[b] Include beam overlap.

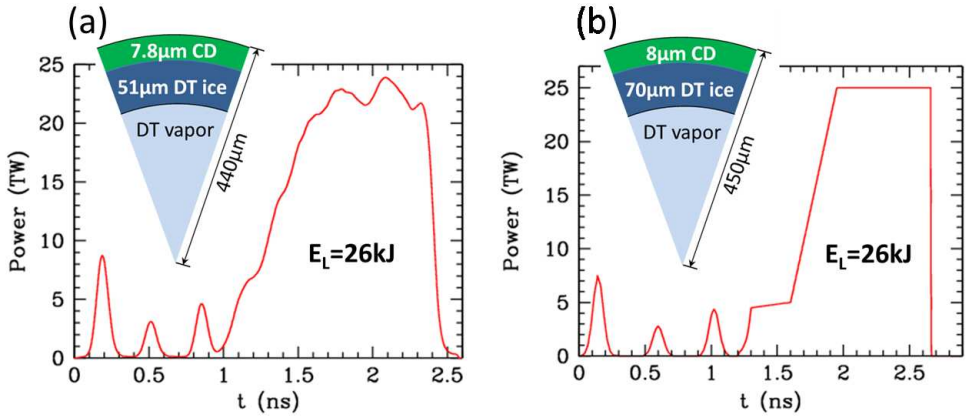

Figure 1: (Color online) Cryogenic DT capsule and laser pulse used in OMEGA shot 78378 (a) and R75 design (b). The DT-ice shell is overcoated by the thin plastic (CD) ablator. The interior of the shell is filled with a DT vapor. The pulse consists of three pickets that launch shocks controlling the shell adiabat and gradually rising 1-ns main drive pulse with a step pre-pulse.

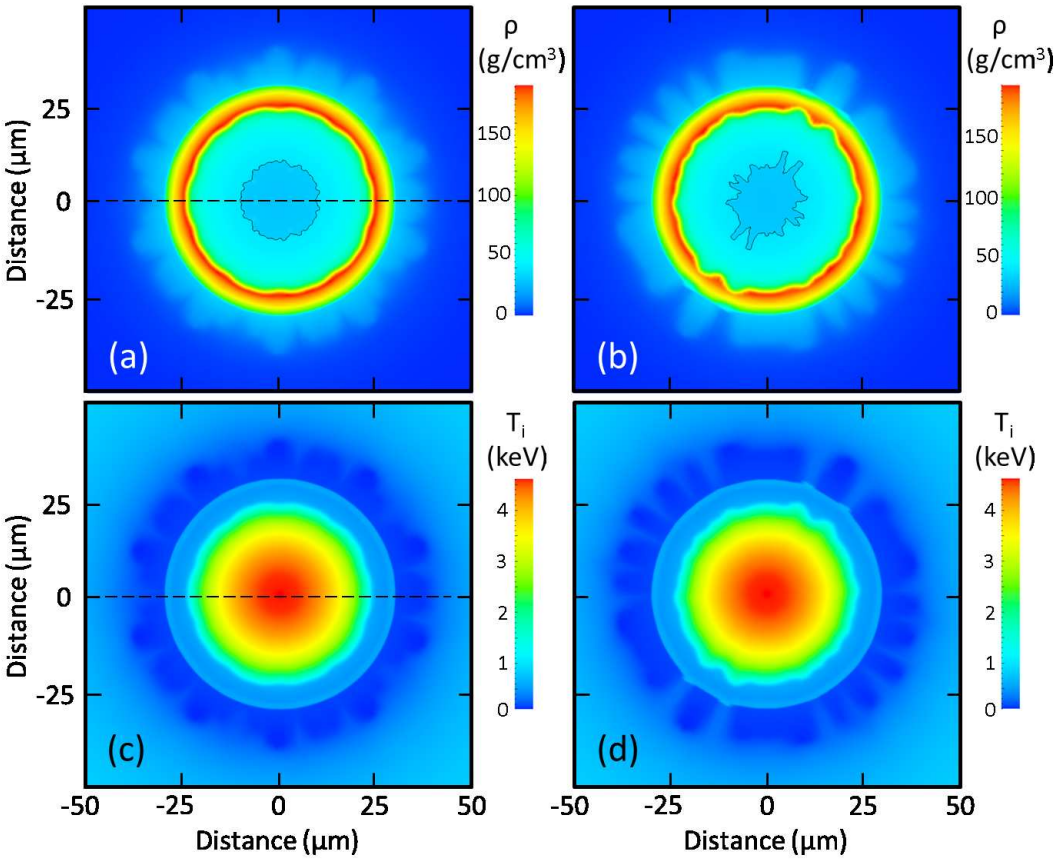

Figure 2: (Color online) 3D model of shot 78378 at the peak neutron production, $t = 2.57$ ns. This model assumes perturbations because of the OMEGA beam overlap (Model A1, see Table 1). (a) and (c) show the equatorial cross-sections, and (b) and (d) show the meridional cross-sections at $\phi = 0$ of the distributions of the density [(a) and (b)] and ion temperature [(c) and (d)]. The dashed lines in (a) and (c) indicate the location of the cross-sections in (b) and (d), respectively. The solid black line in (a) and (b) shows the interface between the plasmas formed by the original DT-vapor and DT-ice.

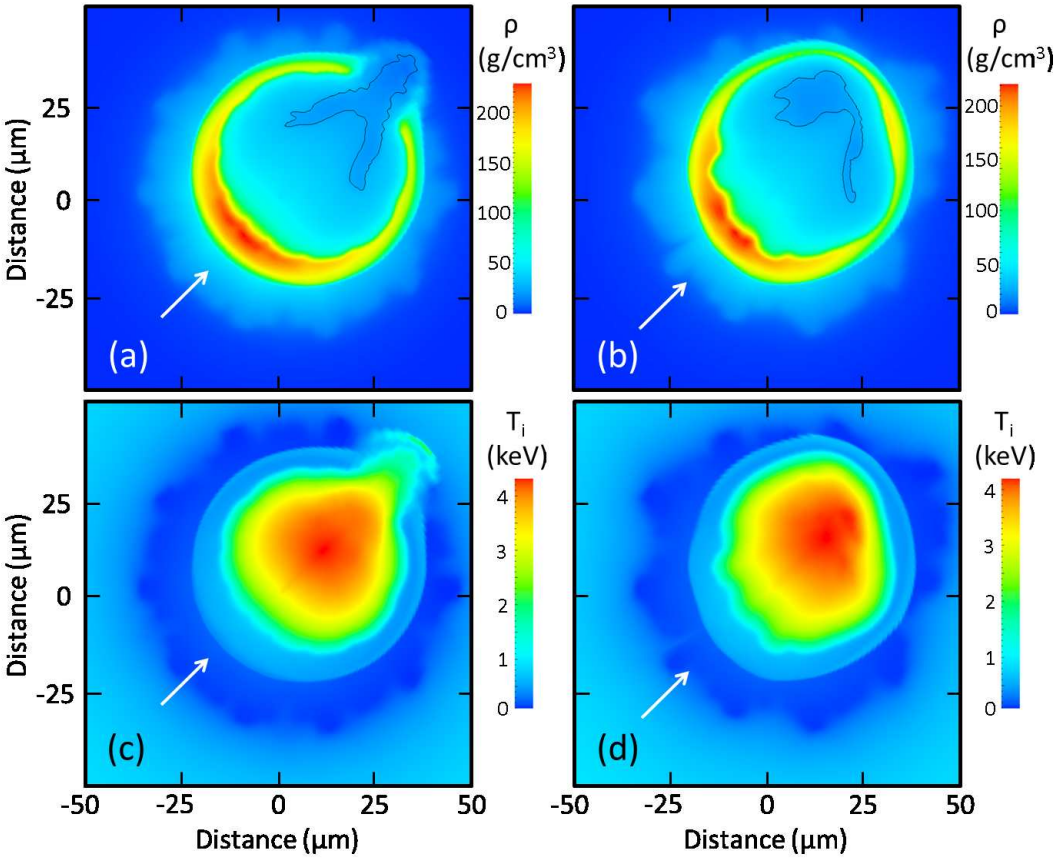

Figure 3: (Color online) Equatorial distributions of the density and ion temperature in Models A2 [(a) and (c), respectively] and A3 [(b) and (d), respectively] at the peak neutron production, $t = 2.57$ ns. The models assume a 10-μm offset in the equatorial plane. The direction of the offset is indicated by white arrows. The initial target center is at (0,0). Model A3 assumes perturbations shown in Table 1. For other notations, see Fig. 2.

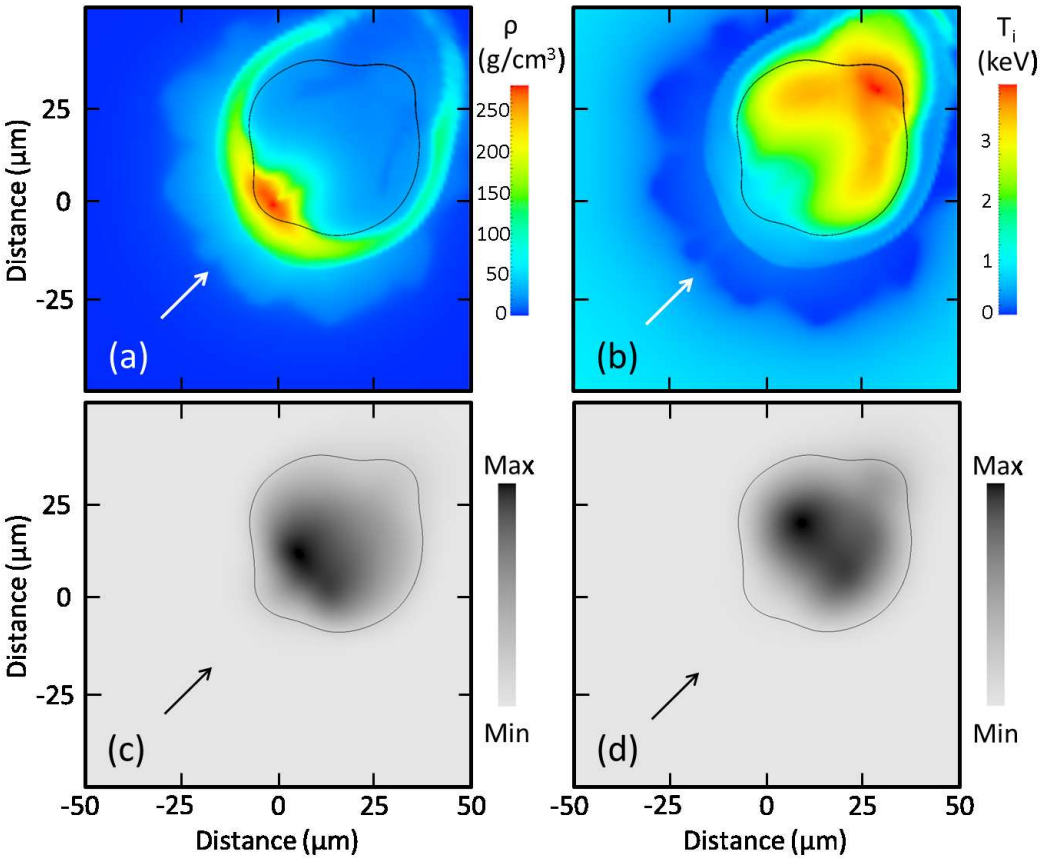

Figure 4: (Color online) Equatorial distributions of the density (a) and ion temperature (b) in Model A7 at the peak neutron production, $t = 2.57$ ns. (c) Polar view in 4- to 8-keV x-rays at the same time. (d) Time-integrated polar view in DT neutrons. The direction of the 20-μm target offset is indicated by arrows. The initial target center is at (0,0). The black contour is the 17% contour of the maximum x-ray fluency in (c).

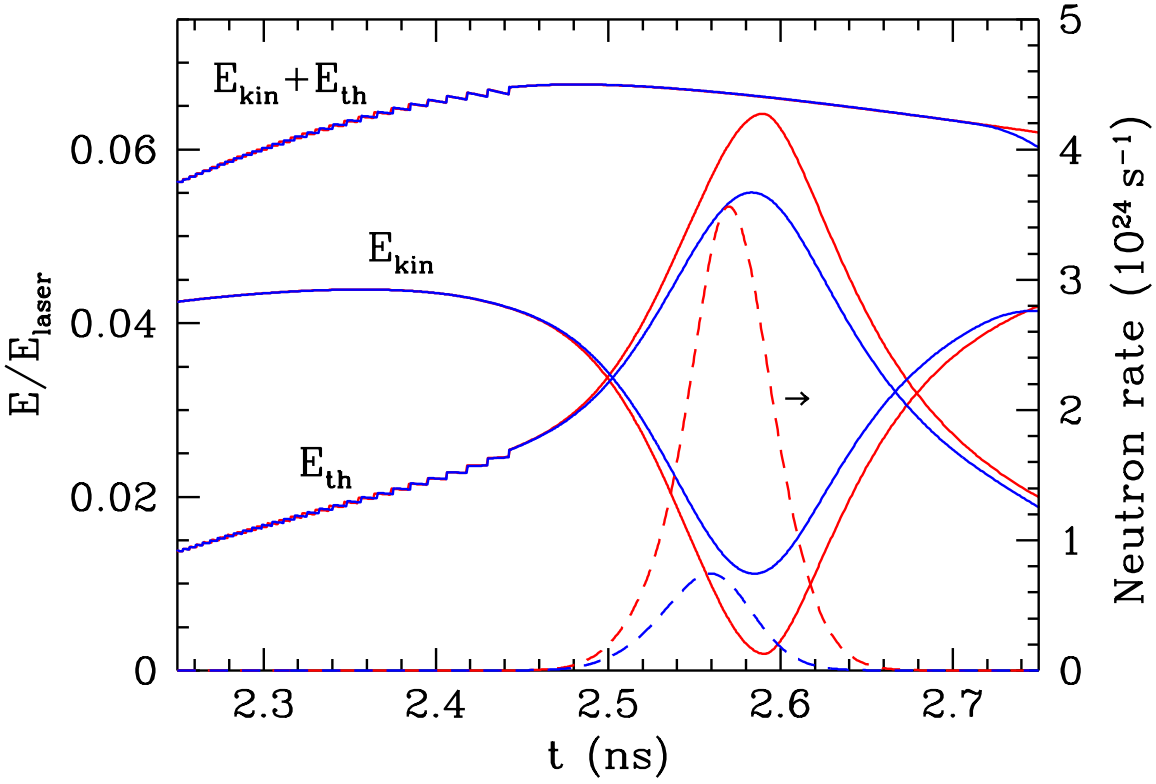

Figure 5: (Color online) Evolution of the kinetic, thermal, and total (kinetic plus thermal) energies in Models A0 (solid red lines) and A7 (solid blue lines). These energies are calculated within the central spherical volume of the radius of 200 μm. The dashed lines show the corresponding neutron rates (right axis).

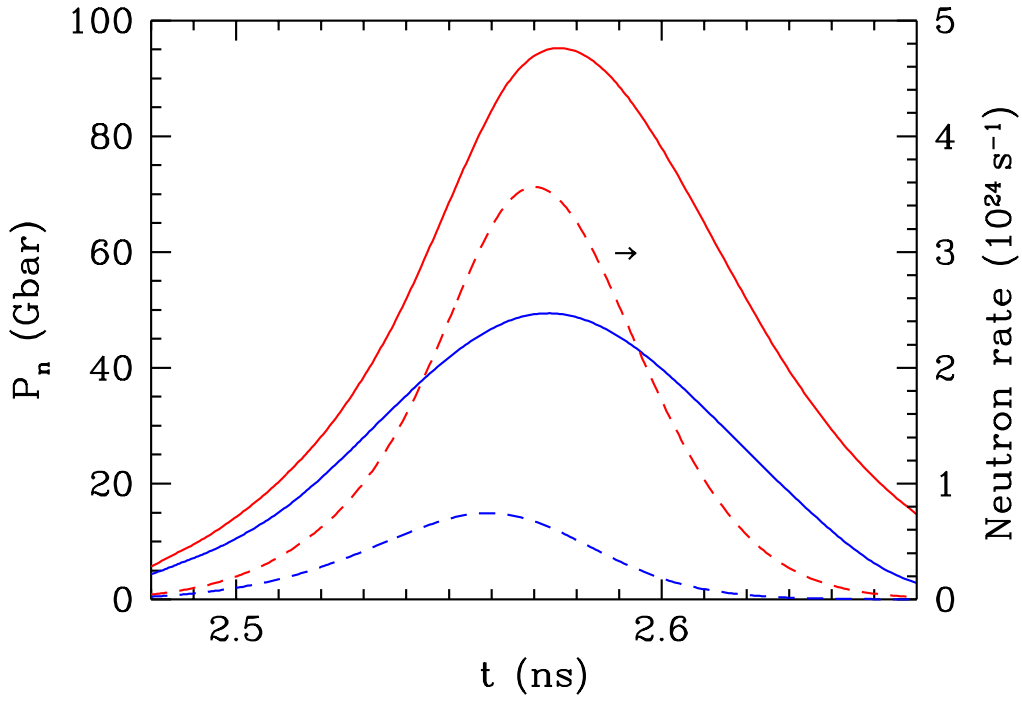

Figure 6: (Color online) Evolution of the neutron averaged pressure in Models A0 (solid red line) and A7 (solid blue line). The dashed lines show the corresponding neutron rates (right axis).

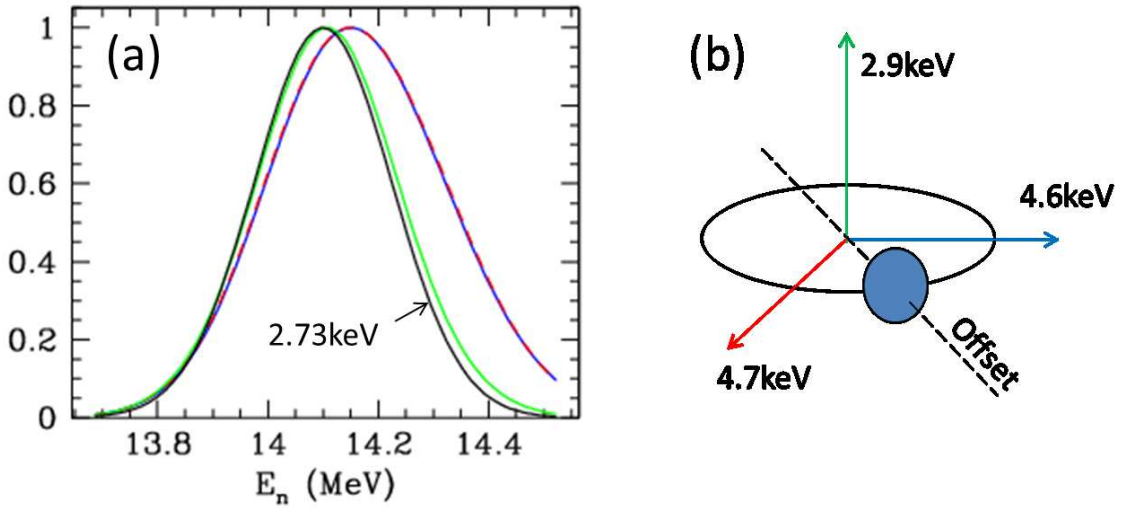

Figure 7: (Color online) (a) Simulated DT neutron spectra in Model A7. The black line shows the spectrum corresponding to $(T_i)_n = 2.73$ keV and without the effect of bulk motion. The green, blue, and dashed red lines present spectra calculated in three different directions indicated in (b) and including this effect. The colors of the arrows in (b) correspond to the color lines in (a). The temperatures in (b) are the inferred ion temperatures in the corresponding directions.

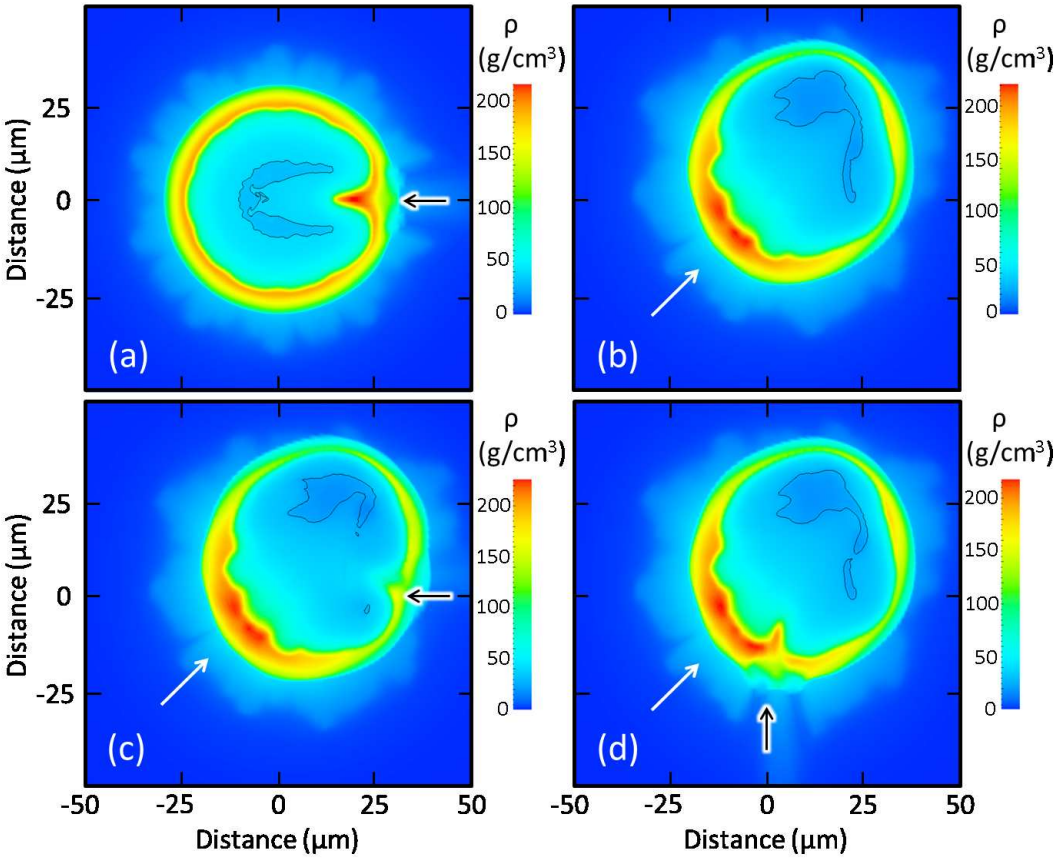

Figure 8: (Color online) 3D models of shot 78378 assuming perturbations from the mount stalk and OMEGA beam overlapping (a), perturbations as in Model A3 without stalk (b) and perturbations as in Model A3 plus perturbations from the stalk at two different locations (c) and (d). The equatorial cross-sections of the density distributions are shown at peak neutron production, $t = 2.57$ ns. The white arrows indicate the direction of a 10-μm target offset and the black arrows indicate the locations of the stalk. For other notations, see Fig. 2.

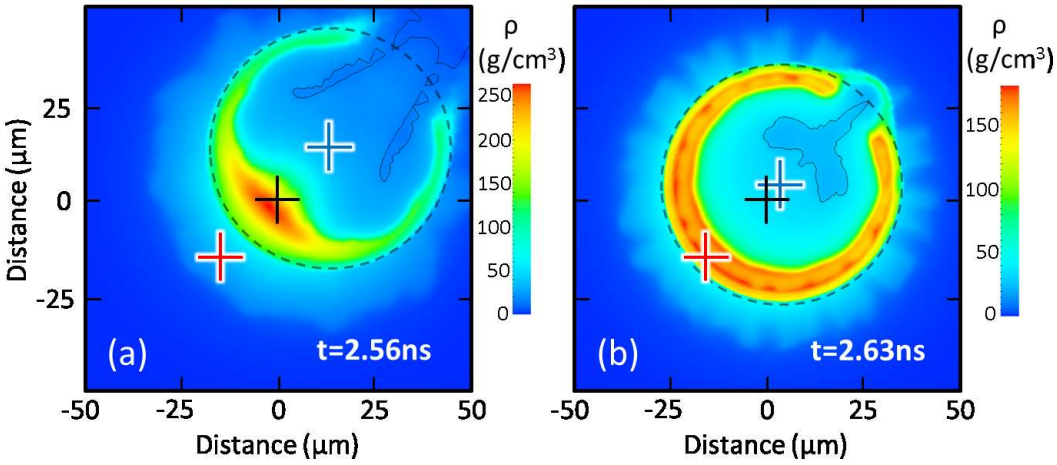

Figure 9: (Color online) Comparison of simulations of shot 78378 using the Spitzer heat transport and CBET (a), and the flux-limited heat transport without CBET (b). The images show the distribution of the density at the equatorial plane at the peak neutron production, $t = 2.56$ and 2.63 ns, respectively. The simulations assume perturbations because of the OMEGA beam overlap and 20-μm target offset in the equatorial plane. The black and red crosses indicate the initial target and offset beam pointing centers, respectively. The circles shown by the black dashed lines approximately indicate the position of implosion shells and the blue crosses present the centers of these circles. For other notations, see Fig. 2.

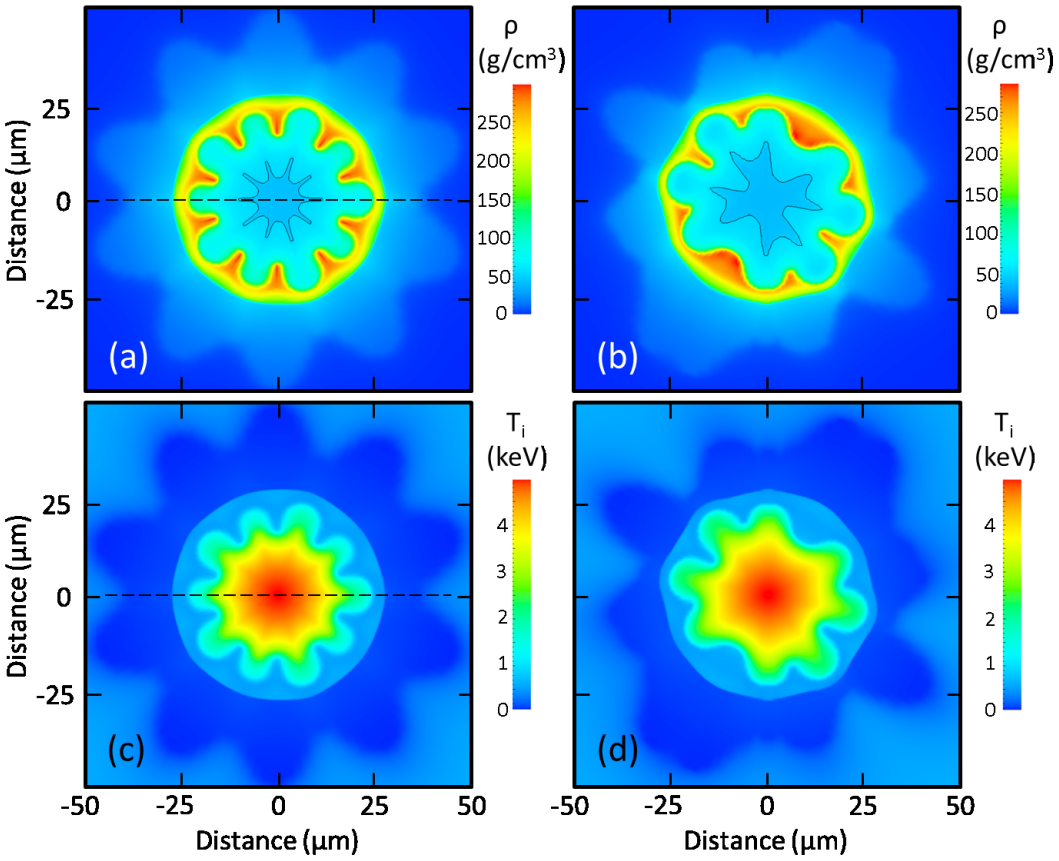

Figure 10: (Color online) 3D model of the R75 design at the peak neutron production, $t = 2.94$ ns. The model assumes perturbations because of the OMEGA beam overlap (Model B1, see Table 2). For notations, see Fig. 2.

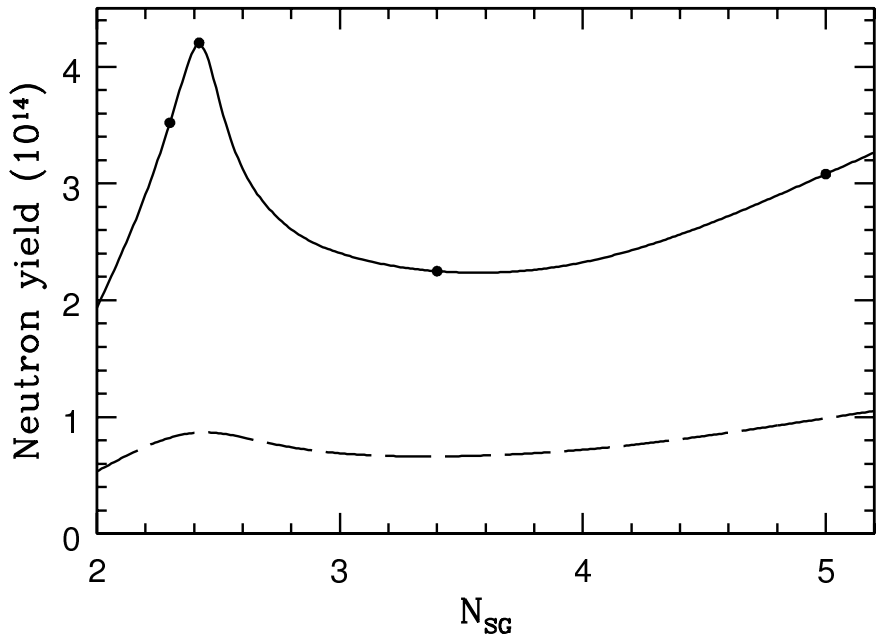

Figure 11: Simulated neutron yield of the R75 design as a function of the beam supergaussian index N_{SG}. The solid line represents models assuming perturbations only because of the OMEGA beam overlap. The solid circles indicate the cases of N_{SG} = 2.3, 2.42, 3.4, and 5.0, which correspond to images in Fig. 12. The dashed line represents models, which add perturbations from other sources (see the text).

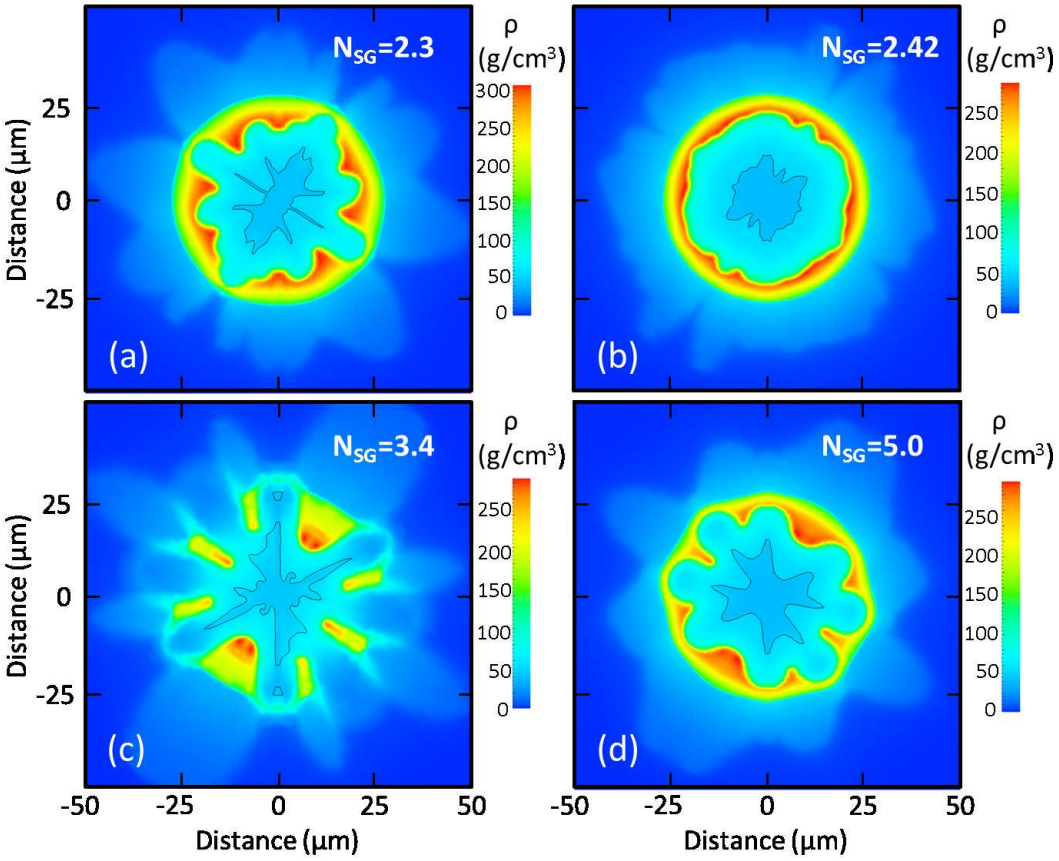

Figure 12: (Color online) Meridional cross-sections of the distribution of the density of the R75 design for $N_{SG} = 2.3$ (a), 2.42 (b), 3.4 (c), and 5.0 (d). The implosions are shown at the peak neutron production and assume perturbations only because of the OMEGA beam overlap. For notations, see Fig. 2.

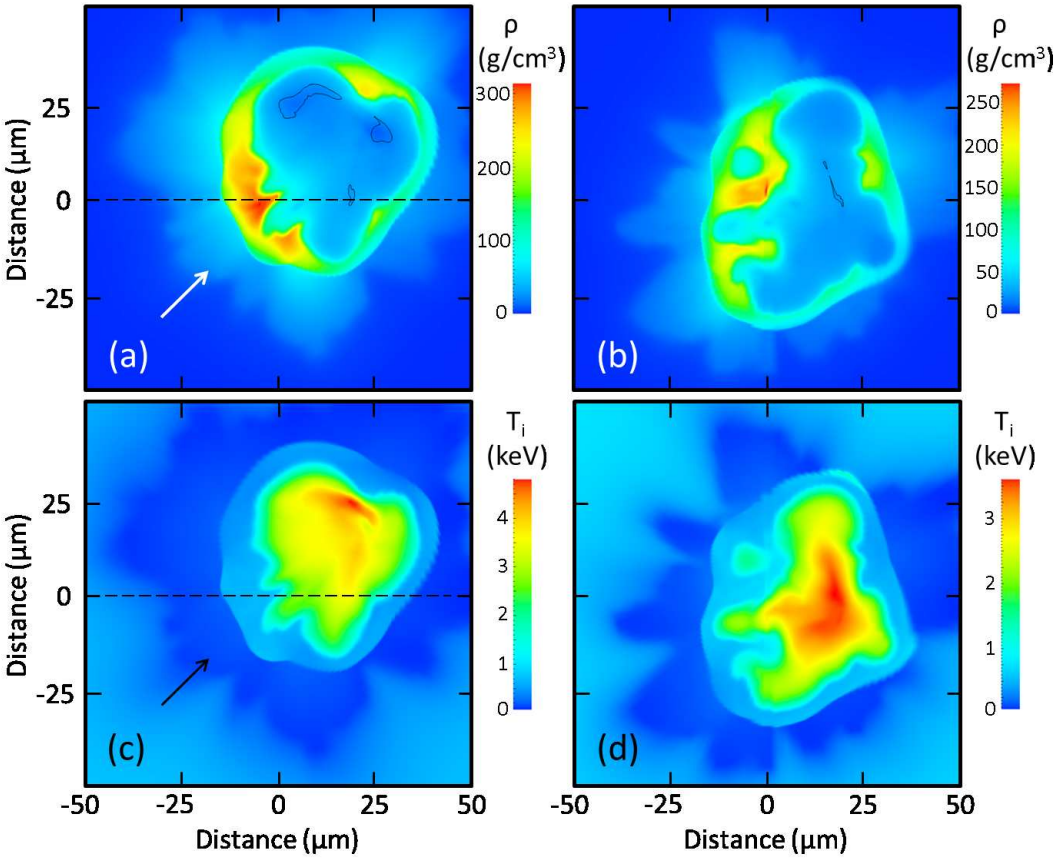

Figure 13: (Color online) 3D model of the R75 design with various perturbations (see the text) at the peak neutron production, $t = 2.91$ ns. The simulations assume $N_{SG} = 2.42$. For notations, see Fig. 2.

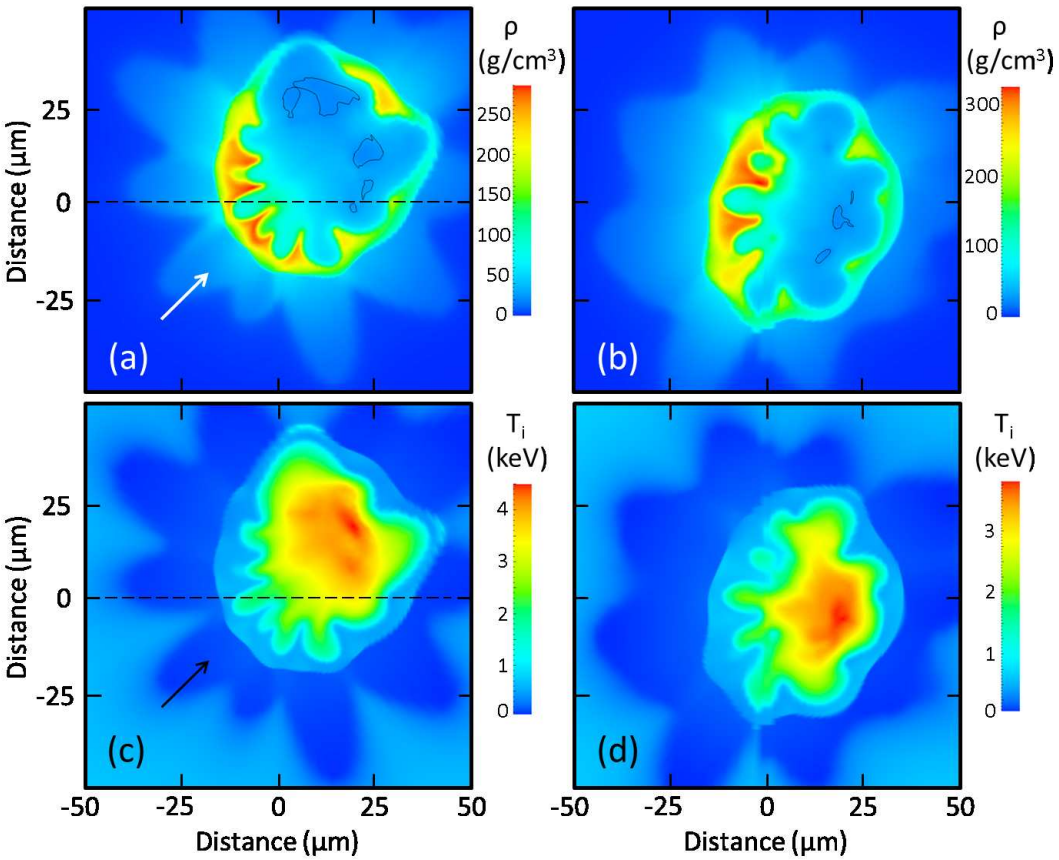

Figure 14: (Color online) Same as in Fig. 13, but at $t = 2.93$ ns and assuming $N_{SG} = 5.0$.

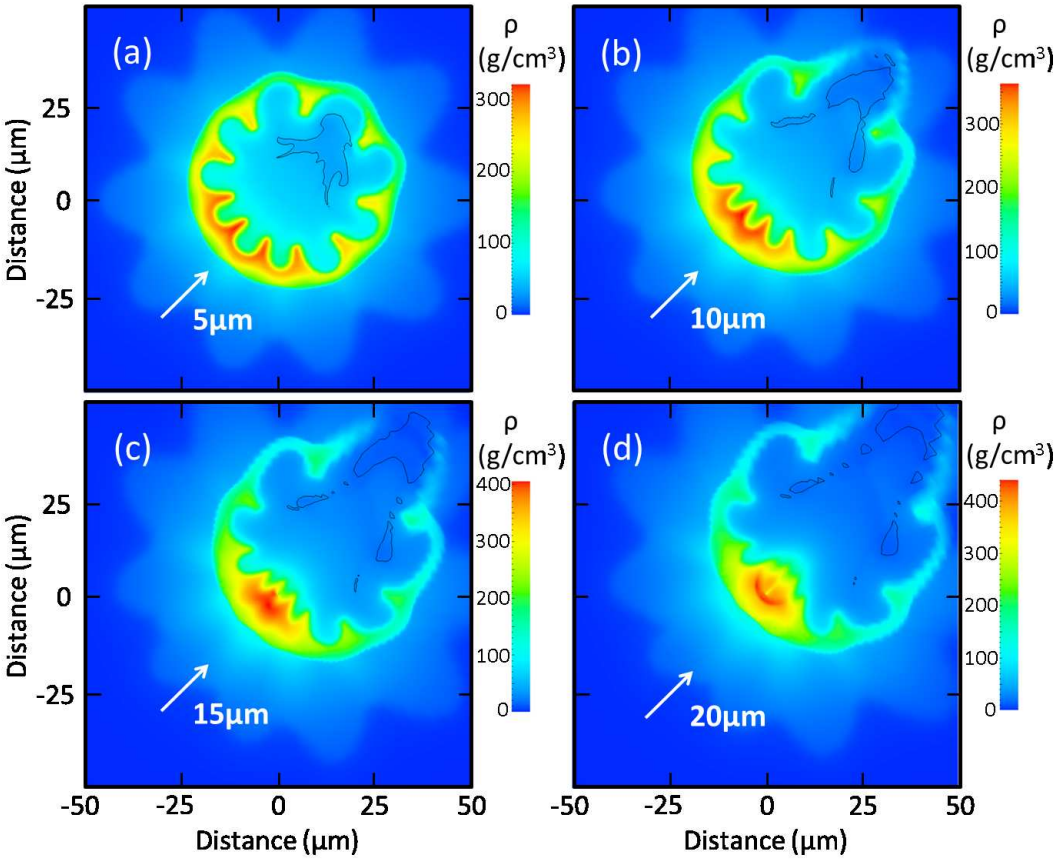

Figure 15: (Color online) Equatorial cross-sections of the distribution of the density of the R75 design assuming the target offset of 5 μm (a), 10 μm (b), 15 μm (c), and 20 μm (d). The implosions are shown at the peak neutron production and assume perturbations because of the OMEGA beam overlap. For notations, see Fig. 2.

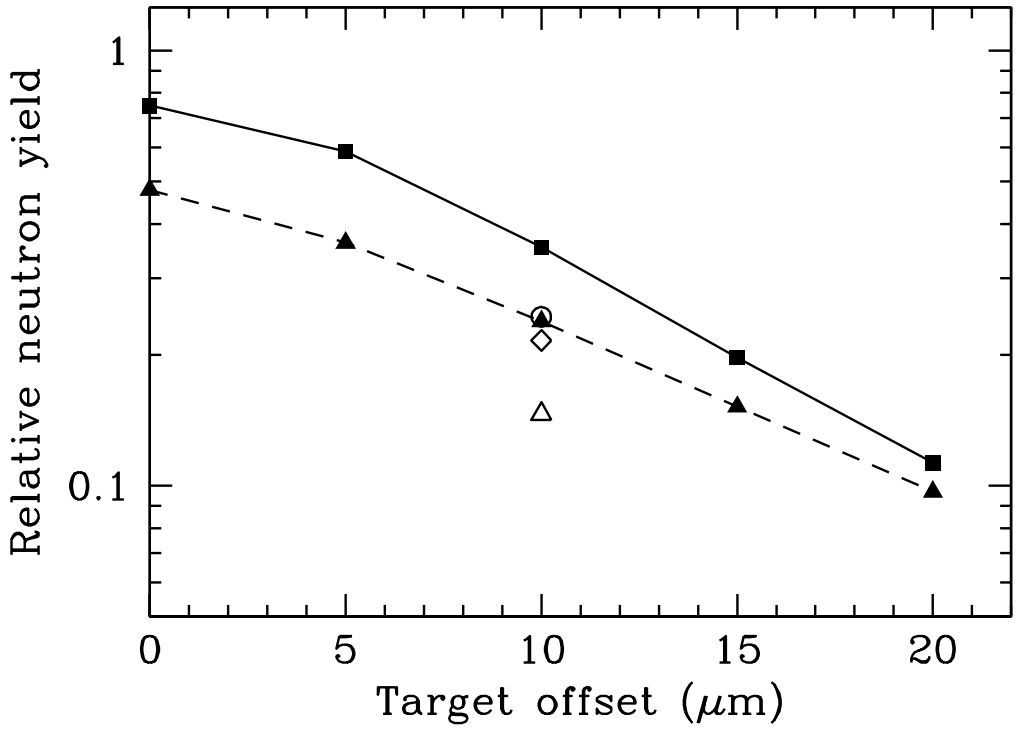

Figure 16: Relative neutron yield in the R75 design depending on the target offsets. The implosions assume perturbations because of the OMEGA beam overlap (solid squares) and adding perturbations because of a 10% σ_{rms} beam imbalance, 10 μm σ_{rms} beam mispointing, and 5 ps σ_{rms} beam mistiming (solid triangles). The open triangle, diamond, and circle correspond to the models with the perturbations, in which the beam imbalance, mistiming, and mispointing are consequently increased by a factor of 2 (Models B4, B5, and B6, see Table 2).

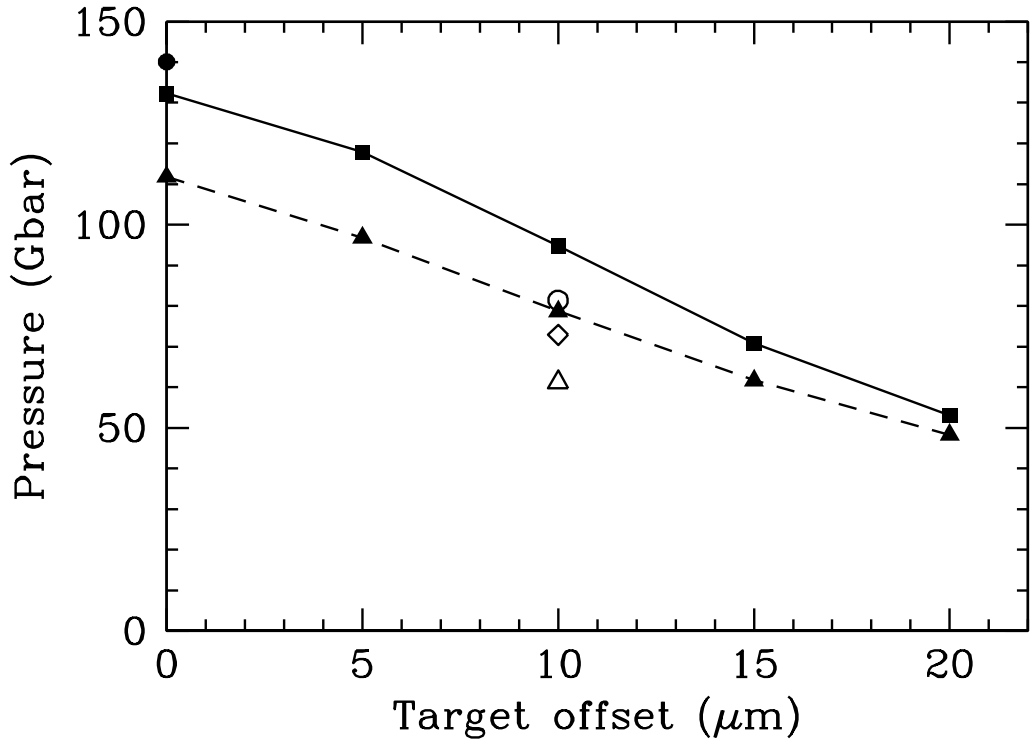

Figure 17: Hot spot pressure P_{hs} in the R75 design depending on the target offsets. The solid circle shows the pressure in the uniform implosion. For other notations, see Fig. 16.